

TECHNICAL UNIVERSITY OF CRETE
ELECTRONIC AND COMPUTER ENGINEERING DEPARTMENT
TELECOMMUNICATIONS DIVISION



Energy Harvesting and Sensing for Backscatter Radio

by

Spyridon-Nektarios Daskalakis

A THESIS SUBMITTED IN PARTIAL FULFILLMENT OF
THE REQUIREMENTS FOR THE DIPLOMA THESIS OF

ELECTRONIC AND COMPUTER ENGINEERING

October 3, 2014

THESIS COMMITTEE

Associate Professor Aggelos Bletsas, *Thesis Supervisor*

Assistant Professor Eftichios Koutroulis

Associate Professor Antonios Deligiannakis

Abstract

Nowadays, energy harvesting has become an increasingly attractive research topic due to the proliferation of radio frequency emitters. The goal is to collect unused ambient RF energy and supply small sensors with power. In the first part, an efficient, low-cost and low-complexity rectenna-grid is analysed, fabricated and measured, for low-power RF input and RF density. Despite the fact that a lossy and low-cost FR-4 substrate was used, the RF-to-DC rectification efficiency of 20.5 % and 35.3 % is achieved at -20 and -10 dBm power input, respectively. The rectenna was connected to a custom DC-to-DC converter and the open voltage was increased from 298 mV to 1.4 V, charging a 1 mF capacitor at 37 min.

Monitoring, environmental variables such as soil moisture, relative humidity, etc. with wireless sensor networks (WSNs) is invaluable for precision agriculture applications. However, the effectiveness of existing low-power, conventional (e.g. ZigBee-type) radios in large-scale deployments is limited by power consumption, cost and complexity constraints. While the existing WSN solutions employing non-conventional, scatter-radio principles have been restricted to communication ranges of up to a few meters, a novel joint analog design of wireless transmitter (tag) with scatter radio and extended communication ranges is presented in this thesis. Two sensing elements that can be connected with the tag were implemented, a soil moisture sensor and a plant signal sensor. The network tag with the soil moisture sensor was selected to be evaluated in terms of accuracy and communication range. The design is based on a custom microstrip capacitor, exploits bistatic analog scatter radio principles and is able to wirelessly convey soil moisture percentage by mass (% MP) with RMS error of 1.9%. Power consumption and communication range is on the order of 100 μW and 100 meters, respec-

tively. It is tailored for ultra-low cost (5 Euro per sensor) agricultural sensor network applications for soil moisture.

Thesis Supervisor: Associate Professor Aggelos Bletsas

To my family.

Table of Contents

| | |
|---|----|
| Table of Contents | 5 |
| List of Figures | 7 |
| List of Tables | 10 |
| 1 Introduction | 11 |
| 1.1 State of the Art | 13 |
| 2 Energy Harvesting Design | 16 |
| 2.1 RF-to-DC Power Converter | 16 |
| 2.1.1 Diode Rectifier Theory | 16 |
| 2.1.2 Impedance Matching Theory | 18 |
| 2.2 Rectifier | 18 |
| 2.2.1 Design and Analysis | 19 |
| 2.2.2 Rectifier Measurements | 22 |
| 2.3 Rectenna Grid | 23 |
| 2.3.1 Rectenna Design and Radiation Pattern | 24 |
| 2.3.2 Rectenna Efficiency | 25 |
| 2.3.3 The DC-to-DC Converter | 28 |
| 3 Sensing for Scatter Radio Tag | 33 |
| 3.1 Scatter Radio Communication | 33 |
| 3.2 Scatter Radio Sensing Topology | 34 |
| 3.3 Analog Frequency Modulator | 36 |
| 3.4 RF Front-End | 39 |
| 3.4.1 Analysis | 39 |
| 3.4.2 Design and Fabrication | 40 |

| | | |
|----------|--|-----------|
| 3.5 | Soil Moisture Sensor | 41 |
| 3.5.1 | Theory | 42 |
| 3.5.2 | Sensor Design | 43 |
| 3.5.3 | Simulation | 45 |
| 3.5.4 | Fabrication and Insulation | 46 |
| 3.5.5 | Measurements | 47 |
| 3.6 | Plant Signal Sensor | 48 |
| 3.6.1 | Analysis | 48 |
| 3.6.2 | Circuit Design | 49 |
| 3.6.3 | Fabrication and Measurements | 51 |
| 3.7 | Power Supply | 52 |
| 3.8 | Multiple Access | 56 |
| 3.9 | Sensor Node Construction | 58 |
| 3.10 | Receiver | 59 |
| 3.11 | Calibration | 60 |
| 3.12 | Ranges and Cost | 62 |
| 3.13 | Testbed | 62 |
| 4 | Conclusions | 65 |
| 4.1 | Conclusion | 65 |
| 4.2 | Future Work | 66 |
| | Bibliography | 73 |

List of Figures

| | | |
|------|---|----|
| 2.1 | (a) Diode series equivalent model, (b) diode parallel equivalent model, (c) simple diode detector. | 16 |
| 2.2 | Two-input microstrip rectifier-grid design (top layer). | 18 |
| 2.3 | The fabricated rectifier. | 19 |
| 2.4 | Γ_{in} coefficient for two ports at 868 MHz. | 20 |
| 2.5 | Rectifier efficiency versus total power input. | 21 |
| 2.6 | Rectifier efficiency versus frequency for different power inputs. | 22 |
| 2.7 | Rectifier efficiency versus load for different power inputs. | 23 |
| 2.8 | Reflection coefficient of the bow-tie antenna. | 24 |
| 2.9 | The proposed rectenna-grid consisting of two identical bow-tie antennas. | 25 |
| 2.10 | The estimated rectenna realized gain. Only one antenna was radiated and the other, with the rectifier, acted as parasitic elements. | 26 |
| 2.11 | Rectenna topology at far-field. | 27 |
| 2.12 | Rectenna measured efficiency. | 28 |
| 2.13 | Measured voltage across the 5 k Ω load. | 29 |
| 2.14 | Efficiency versus ambient power density. | 30 |
| 2.15 | The power at the load versus ambient power density. | 31 |
| 2.16 | Autonomous low-voltage and ultra-low power converter schematic with $C_1 = C_2 = 1$ nF and $C_{out} = 1$ mF. | 31 |
| 2.17 | The fabricated rectenna and the DC-to-DC converter. | 32 |
| 3.1 | Scatter radio communication principles: The low power RF switch alternates the termination loads (Z_1 and Z_2) of the antenna with frequency F_{sw} . When a carrier is equal with frequency F_c , two sub-carriers appear, with frequencies $F_c \pm F_{sw}$ | 33 |

| | | |
|------|--|----|
| 3.2 | Bistatic backscatter sensor network architecture. Low-cost emitter produce the carrier signal which is modulated by sensor nodes and finally, the reflected signal is received by a software defined radio (SDR) reader. | 34 |
| 3.3 | Sensor/tag circuit diagram | 35 |
| 3.4 | The astable multivibrator circuit with 5 V power supply. | 36 |
| 3.5 | Output (blue) voltage and timing capacitor C (yellow) voltage. | 38 |
| 3.6 | Γ_i s on the Smith chart. | 40 |
| 3.7 | Front-end coplanar waveguide structure. | 41 |
| 3.8 | Schematic diagram of cross section of FEF soil moisture sensor. [1] | 44 |
| 3.9 | Soil moisture sensor schematic diagrams. | 45 |
| 3.10 | ADS 3D Preview of sensors electrodes, the ports are used for model simulation. | 45 |
| 3.11 | Capacitance(pf) vs Number of drive fingers. | 47 |
| 3.12 | Fabricated sensors with different types of insulation. | 48 |
| 3.13 | Instrumentation amplifier schematic. | 49 |
| 3.14 | Fabricated sensor and calibration characteristic. | 51 |
| 3.15 | Current consumption at R_1 loop with (third graph) and without (second graph) the switch. | 52 |
| 3.16 | Power consumption of ten tags. | 55 |
| 3.17 | FDMA Scheme Overview. | 56 |
| 3.18 | Sensor network spectrum for sensors 1, 2, 3, 4. Sensors 1, 2 and 3, 4 occupy a bandwidth of 1 and 5 kHz, respectively. | 57 |
| 3.19 | Sensor network spectrum for sensors 1, 2. Harmonics and spurious signals are observed. | 58 |
| 3.20 | Fabricated circuit board with capacitive sensor, power supply circuit and timer module circuit. | 59 |
| 3.21 | Left: Installation of the sensor on an avocado plant with utilization of “IP65”-rated enclosures. Right: Close-up view of the fabricated sensor. | 60 |
| 3.22 | Measured soil moisture (%) characteristic and fitted function versus frequency. | 61 |

| | | |
|------|--|----|
| 3.23 | Indoor setup testbed of the bistatic analog backscatter architecture. | 63 |
| 3.24 | Soil moisture measurements of two sensors for 3 hours. | 64 |
| 4.1 | Schematic of plant signal sensor. | 68 |
| 4.2 | PCB layout of plant signal sensor. | 69 |
| 4.3 | Schematic of timer module, soil moisture sensor and power supply circuit. | 70 |
| 4.4 | PCB layout of timer module, soil moisture sensor and power supply circuit. | 71 |
| 4.5 | Schematic of RF front-end. | 71 |
| 4.6 | PCB layout of RF front-end. | 71 |
| 4.7 | The various tag and sensor prototypes that were fabricated. | 72 |

List of Tables

| | | |
|-----|--|----|
| 1.1 | RF-to-DC conversion efficiency versus power input/density and frequency | 14 |
| 3.1 | Example of three tags with different duty cycle D | 55 |
| 4.1 | Plant signal sensor bill of materials. | 67 |
| 4.2 | Tag bill of materials. | 67 |

Chapter 1

Introduction

With the growing popularity and applications of large-scale, sensor-based wireless networks (e.g., structural health monitoring, human health monitoring, agricultural monitoring), the need to adopt inexpensive, green communications strategies is of paramount importance. One approach is to deploy a network comprising self-powered tags/nodes/sensor nodes¹ that can harvest ambient energy from a variety of natural and man-made sources for sustained network operation [2]. This instrument can potentially lead to significant reduction in the costs associated with replacing batteries periodically. Moreover, in some deployments, owing to the sensor node location, battery replacement may be both practically and economically infeasible, or may involve significant risks to human life. Thus, there is a strong motivation to enable an off-the-shelf wireless sensor network (WSN) with energy harvesting capability that would allow a sensor node to replenish part or all of its operational costs, thereby taking the first steps towards realizing the vision of a perennially operating network.

The concept of wireless energy harvesting and transfer is not new, rather it was demonstrated over 100 years ago by Tesla [3]. In recent times, radio frequency identification (RFID) technology is a clear example of wireless power transmission, where such a tag operates using the incident radio frequency (RF) power emitted by the transmitter [4]. However, there are limitations in directly porting these approaches to WSN scenarios: the former cannot be scaled down for the small sensors, while RFID is unable to generate enough energy to run the local processing tasks on the node, such as powering a micro-controller or a timer. However, given the recent advances in energy efficiency for the circuit components of a rectifier (say, diodes that require less

¹In line with standard RFID terminology, the terms “tags”, “nodes” and “sensor nodes” will be used interchangeably.

forward voltage threshold), and the low-power operation modes supported by the sensor node itself (say, sleep mode consuming only μWs), there is a visible need for revisiting energy harvesting circuit design that, can successfully operate a sensor node.

In order to implement a high efficiency design for low-power input, a rectenna-grid was utilized. It consists of two low-cost and low-complexity single circuits [5] and a pair of custom antennas. RF-to-direct current (DC) efficiency of 20.5 % is achieved, for total power input -20 dBm, or equivalently, for power density $0.019 \mu\text{W}/\text{cm}^2$, as explained bellow. Next, the rectenna was connected to a DC-to-DC converter in order to enhance the open circuit DC voltage, from 298 mV to 1.4 V. Finally, a 1 mF capacitor was charged in 37 min and the stored energy of 0.98 mJ could supply a wireless sensor node with 20 mW power consumption, rate 1 kbps and word-length 20 bits (0.4 mJ per packet).

As mentioned above, the WSNs have become a field of tremendous research interest due to a rich and diverse variety of applications, including large-scale environmental sensing [6, 7]. Environmental variables (e.g., temperature, relative humidity, soil moisture) monitoring is invaluable for precision agriculture applications. However, a common WSN platform typically consists of a micro-controller unit (MCU) and an active radio for sensor data transmission. Despite the fact that literature develops algorithms and protocols for ultra large-scale networks, hundreds of nodes, large-scale outdoor demonstration deployments are rare. Work in [8] demonstrated one of the very few examples of a large-scale, outdoor deployment. However each node *cost* was on the order of 50 €, amplifying the overall network cost and thus, restricting scaling opportunities. Additionally, work in [9] studied the complexity of cross-layer application development in typical WSN platforms and emphasized the difficulty to implement software for robust sensor networks. On the other hand, recent work relevant to backscatter radio has shown significant progress towards low-cost and low-power sensing (e.g. work in [10–13]). Backscatter communication can be implemented with a single antenna, a switching transistor and logic that controls that switch, such that the sensor’s antenna is alternatively terminated at different loads.

However, inductive coupling and/or monostatic battery-less setups result in short communication range, limiting the use of backscatter radio for broad-area environmental sensing.

This part of work offers a novel joint analog design of wireless transmitter (tag) with scatter radio and extended communication ranges. Two sensing elements that can be connected with the tag, were implemented, a soil moisture sensor (3.5) and a plant signal sensor (3.6). The network tag with the soil moisture sensor was selected to be evaluated in terms of accuracy and communication range and a proof-of-concept soil moisture sensor is demonstrated. The design is based on a custom microstrip capacitor, exploits bistatic analog scatter radio principles and is able to wirelessly convey soil moisture percentage by mass (% MP) with RMS error of 1.9%, power consumption and communication range on the order of $100 \mu W$ and 100 meters, respectively. It is tailored for ultra-low cost (5 € per sensor) soil moisture agricultural wireless networks.

1.1 State of the Art

Energy harvesting has become an increasingly attractive research topic due to the proliferation of radio frequency emitters. The goal is to collect unused ambient RF energy and supply with power small electrical devices, such as sensors nodes. Three decades have passed since the rectenna (i.e. antenna and rectifier) was first proposed for transformation of RF energy to DC [14]. Recently, considerable research effort has been directed towards high-efficiency. However, most prior art designs operate optimally at *high* input power, e.g. greater than 0 dBm [15–19]. In order to increase the efficiency at *low* power input, e.g. less than 0 dBm [5, 20–26], substrates with low losses [21, 22, 24] or hybrid designs [23] have been used, raising the total cost or the fabrication complexity, respectively. In [20, 25] power is harvested from a Digital TV power station and wide-band efficiency is estimated, while in [26] ambient RF power is collected and the end-to-end efficiency is estimated, as the ratio of the obtained DC energy to the captured RF energy. Table 1.1 presents analytically the achieved efficiency versus input power (or

Table 1.1: RF-to-DC conversion efficiency versus power input/density and frequency

| work | efficiency | power input (dBm) | frequency (MHz) |
|-------------------|------------|----------------------|--------------------|
| [15] | 65 % | 25 | 2450 |
| [16] ¹ | 20 % | 13.27 | 2000 – 18000 |
| [17] | 77.8 % | 10 | 2400 |
| [18] ² | 54 % | 9.54 | 1960 |
| [19] | 40 % | 0 | 2450 |
| [20] | 21 % | −4.74 | 512 – 566 |
| [21] | 56.4 % | −10 | 900 |
| [22] | 50 % | −17.2 | 2450 |
| [23] | 15 % | −20 | 850, 1850 |
| [24] | 15.3 % | −20 | 2450 |
| [5] | 17 % | −20 | 868 |
| [25] | 18.1 % | −20 | 470 – 770 |
| [26] ³ | 40 % | −25.4 | 2110 – 2170 |

¹ $A_{\text{eff}} = A = 18.5 \times 18.5 \text{ cm}^2$, $S = 62 \mu\text{W}/\text{cm}^2$.

² $A_{\text{eff}} = A = 7.5 \times 6 \text{ cm}^2$, $S = 200 \mu\text{W}/\text{cm}^2$.

³The end-to-end efficiency as the ratio of the obtained DC energy to the captured RF energy.

power density) and frequency, for various prior art designs.

About the sensing, dense soil moisture sensors could vastly improve irrigation systems and offer tremendous water savings. Novel soil moisture capacitive sensors have appeared in the literature, typically integrated with a discrete wireless radio module [27], or a discrete processing chip [28], including inkjet fabrication designs of the sensing element. In an effort to achieve extended wireless communication ranges, while reducing the monetary and energy cost, recent work [29], [30] proposed a joint-design of environmental relative humidity sensing. The wireless communicator, based on analog scatter radio, simplifying the radio front-end to a single transistor. Instead of environmental relative humidity, this work offers an improved joint-design of scatter radio and capacitive sensor. Also the plant signal sensor is described

for future installation on the tag. The target goal of this work is a soil moisture percentage (%SM) wireless sensor network with extended ranges, low power and cost.

Chapter 2

Energy Harvesting Design

2.1 RF-to-DC Power Converter

2.1.1 Diode Rectifier Theory

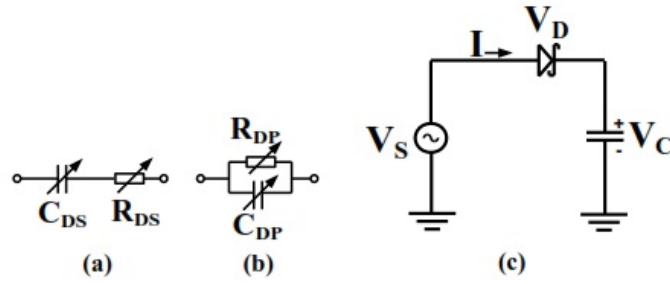


Figure 2.1: (a) Diode series equivalent model, (b) diode parallel equivalent model, (c) simple diode detector.

Rectifier is an electrical device that converts alternating current (AC), which periodically reverses direction, to DC, which flows in only one direction. The RF current in antennas and transmission lines is an example of AC. For power rectification from very low to very high current, semiconductor diodes of various types (junction diodes, Schottky diodes, etc.) are widely used. A junction diode equivalent circuit and simple Schottky diode rectifier are shown in Fig. 2.1. R_{DS} is the diode resultant series resistance, C_{DS} is the diode resultant series capacitance, R_{DP} is the diode resultant parallel resistance, C_{DP} is the diode resultant parallel capacitance, V_S is the sinusoidal source voltage and V_C is the voltage across the capacitor.

The diode capacitive impedance is mainly due to the junction capacitances provided by the metal, its passivation and the semiconductor forming the diode. AC power incident on a forward biased diode input is converted

to DC power at the output. The current-voltage behaviour of a single metal/semiconductor diode is described by the Richardson equation [31] as in (2.1):

$$I = I_S \left(e^{\left(\frac{qV_D}{nKT}\right)} - 1 \right) \quad (2.1)$$

where I is the current through the diode, I_S is the saturation current, q is the charge of an electron, V_D is the voltage across the diode, T is the temperature in degrees Kelvin and K is Boltzmann constant. The voltage equation around the loop can be derived from Fig. 2.1 (c) and is given in (2.2):

$$V_D = V_S - V_C \quad (2.2)$$

Since the same current flows through the diode and the capacitor, one can find the average current through the circuit by integrating (2.1) over a time period. By substituting (2.2) into (2.1), V_C can be expressed in terms of V_S by averaging the diode current to zero. This is given in Equation (2.3) [32]:

$$V_C = \frac{KT}{q} \ln \left[\theta_0 \left(\frac{qV_S}{KT} \right) \right] \quad (2.3)$$

where θ_0 is the series expansion of the sinusoidal source voltage. Equation (2.3) can further be simplified for very small amplitude V_S as (2.4):

$$V_C = \frac{qV_S^2}{4KT} \quad (2.4)$$

Equation (2.4) shows that for a small voltage source, the circuit output voltage is proportional to the square of the input sinusoidal voltage; hence it's so-called square law operation. Extensions of this model for voltage multipliers and other input signals are presented in [33] and [34]. Equation (2.4) further confirms that for low input voltage (power ≤ 10 dBm), an impedance matching network between the source and the diode is necessary to improve the detected output voltage and efficiency.

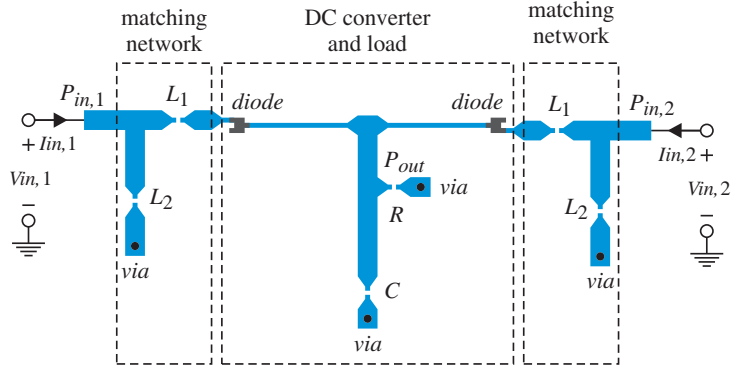


Figure 2.2: Two-input microstrip rectifier-grid design (top layer).

2.1.2 Impedance Matching Theory

The maximum power transfer theorem states that the highest power is transferred to the load when the source resistance is the same as the load resistance. For systems with both resistive and reactive impedances from source and load, the source and the load impedance should be adjusted in a way that they are the complex conjugate of each other through impedance matching. For the purposes of this work, a 50Ω resistive source is chosen as reference for load impedance matching. The antenna which captures the ambient RF signals is tuned to provide this source resistance at resonance for the rectifying circuit in a complete electromagnetic (EM) wireless remote harvester. The load is the resistance of the Schottky diodes and the actual connected resistance (remote sensor node). The specific type of matching network which can be used for complex conjugation depends on the nature of load or source impedance, the desired RF to DC converter functionality and other factors like circuit size, cost, etc.. The response of a matched RF to DC power converter depends on the matching network used as well as the source or load component quality factors and impedances.

2.2 Rectifier

Based on the above section 2.1 a high-efficiency for low-power input, low-cost and low-complexity rectifier (RF to DC power converter) is designed,

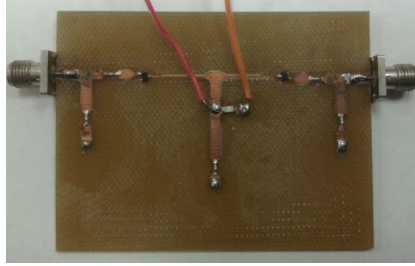


Figure 2.3: The fabricated rectifier.

analyzed and fabricated. In order to decrease the total cost, a lossy substrate is used, although losses reduce efficiency. The efficiency is increased using a single series circuit with a single diode [5], while the total power on load is enhanced through a rectenna-grid design, for low-power density, below $1 \mu\text{W}/\text{cm}^2$.

Specifically, rectification of the received RF power to DC power is achieved using two single series rectifier circuits, consisting of a matching network and a single diode, in each input port. Their outputs are joined together, adding the currents from each diode and finally, feeding the load R . The latter leads to enhancement of the power which is offered to the load, for low-power RF density. The whole geometry is depicted in Fig. 2.2 and 2.3. Low cost Schottky diodes “HSMS-285B” from Avago [35] are used to build the rectifier. The “HSMS-285B” diode can be operated as zero biased with relatively low forward junction potential. This allows the realization of completely passive RF to DC power converters for wireless energy harvesting. The “HSMS-285B” is a single Schottky diode in a “SOT-323” package. Finally, the substrate that is used from the fabrication is (lossy) FR-4 with $\epsilon_r = 4.4$, $\tan \delta = 0.025$, copper thickness $0.35 \mu\text{m}$ and height 1.5 mm .

2.2.1 Design and Analysis

For simulations, Agilent Technologies’ “ADS” software is employed, with harmonic balance and the method of moments solver. Full electromagnetic analysis takes simultaneously into account the losses from the low-cost FR-4, the fringing fields and the non-linear behaviour of the rectifier due to the

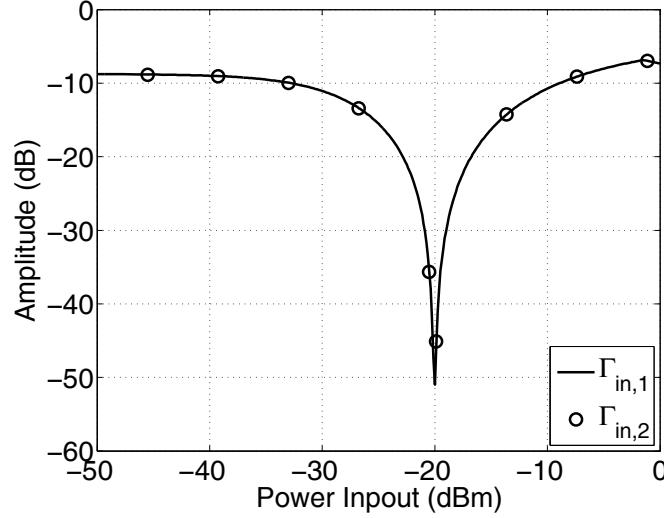


Figure 2.4: Γ_{in} coefficient for two ports at 868 MHz.

diodes. As indicated above (2.1.2), it is assumed that the rectifier ports will be connected to antennas with input impedance equal to 50Ω , while the (low) power input P_{in} , varies from -30 dBm to -10 dBm. The system was chosen to operate at 868 MHz, which is the UHF ISM center frequency in Europe. In order to design the rectifier (i.e. trace dimensions and lumped elements L_i) an optimization procedure was applied. The goal was the minimization of term,

$$\Gamma_{in,1} = \frac{Z_{in,1} - 50}{Z_{in,1} + 50}, \quad (2.5)$$

for power input at port “1”, $P_{in,1}$, -20 dBm at 868 MHz, where

$$Z_{in,1} = \frac{V_{in,1}}{I_{in,1}}, \quad (2.6)$$

is the input impedance at port “1”, with port “2” matched at 50Ω . After simulation, the obtained lumped element values were $L_1 = 27$ nH and $L_2 = 1.5$ nH. The load and capacitor were initially fixed at 5 k Ω and 100 pF, respectively. The results, $\Gamma_{in,i}$, are depicted in Fig. 2.4. It is observed that the two-port rectifier circuit operates (i.e. the reflection coefficient, $\Gamma_{in,i}$, is less than -10 dBm) from about -33 dBm to -9 dBm power input.

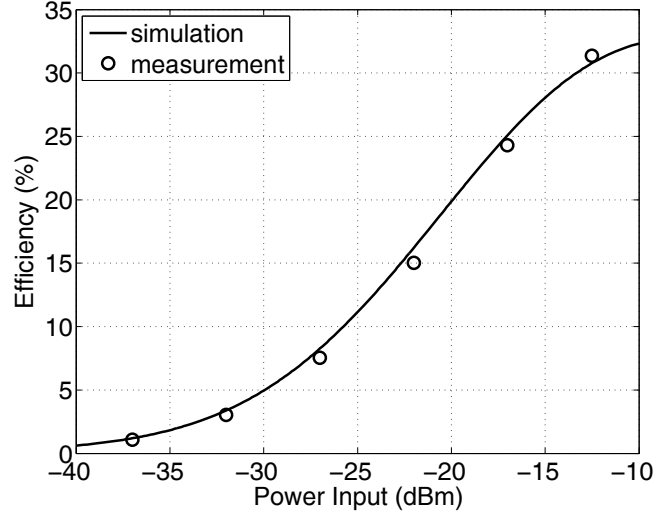


Figure 2.5: Rectifier efficiency versus total power input.

The RF-to-DC efficiency,

$$\eta = \frac{P_{out}}{P_{in}} = \frac{V_R^2/R}{P_{in,1} + P_{in,2}}, \quad (2.7)$$

with P_{in} the total power input at the rectifier, P_{out} the power output at load and V_R the voltage across the load, R , is estimated and depicted in Fig. 2.5. When $P_{in} = -20$ dBm, η is equal to about 20 %, while for $P_{in} = -10$ dBm η reaches the peak of about 32.3 %. It is noted that η is a function of power input, operation frequency and load, hence, the relation between them should be tested. Next, the relation between η , frequency and load will be shown.

Fig. 2.6 shows the rectifier efficiency versus frequency for different power inputs. When $P_{in} = -20$ dBm, it is observed that the rectifier is tuned at 868 MHz, as expected. The highest efficiency 34.3 % is achieved for $P_{in} = -10$ dBm but at 885 MHz. For $P_{in} = -30$ dBm the peak $\eta = 6.2$ % occurs at 850 MHz, while $\eta = 5.2$ % at 868 MHz. It is noted that load was fixed at 5 k Ω .

Finally, the relationship between efficiency and load is studied. Frequency is now fixed at 868 MHz, and the results are shown in Fig. 2.7. It is observed that for $P_{in} = -20$ dBm and R at about 2.7 k Ω , the efficiency is slightly

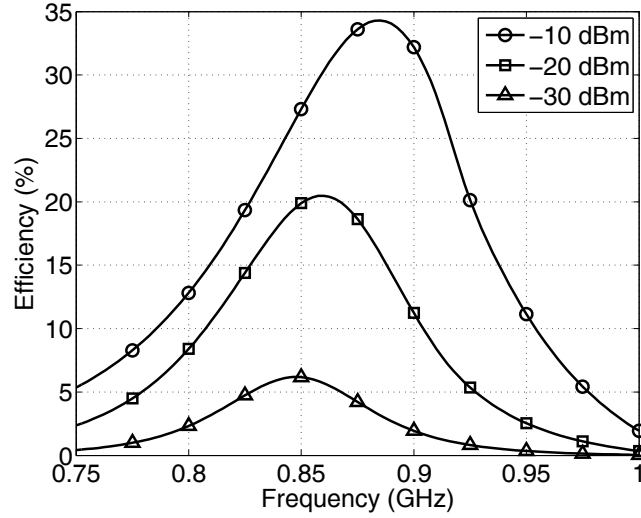


Figure 2.6: Rectifier efficiency versus frequency for different power inputs.

increased from 20 % to 22 %, and for this reason the load remained fixed at 5 k Ω . The maximum $\eta = 39.3$ % occurs for $P_{in} = -10$ dBm when R is equal to about 2.2 k Ω .

2.2.2 Rectifier Measurements

For validation purposes, the rectifier design is fabricated (Fig. 2.3) and tested. A Wilkinson power divider, which was also designed and fabricated, is connected to a signal generator. First, a spectrum analyzer is connected to each divider output, measuring the received power. Next, the spectrum analyzer is removed and power divider outputs were connected to the proposed rectifier. The total power, P_{in} , is considered as the sum of $P_{in,1}$, $P_{in,2}$, which are the two divider output ports. A voltmeter measures the voltage across the load, which is fixed at 5 k Ω . Fig. 2.5 depicts the simulated/measured results. Good agreement between simulation and measurements is observed.

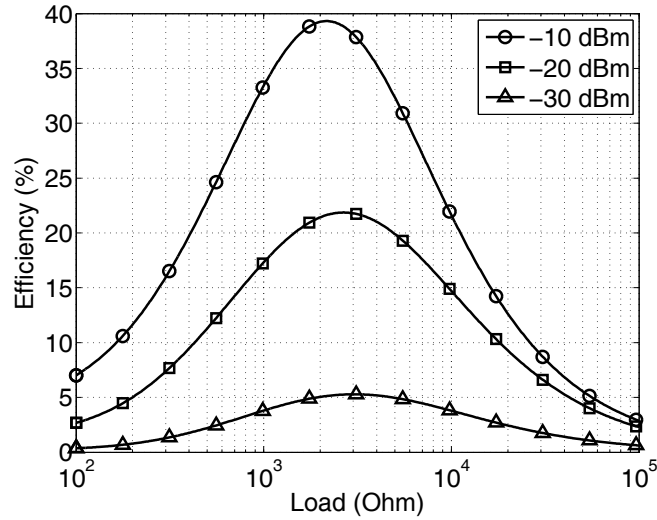


Figure 2.7: Rectifier efficiency versus load for different power inputs.

2.3 Rectenna Grid

A crucial rectenna parameter, apart from the efficiency, is the amount of power offered at the load. The ambient power density is usually below $1 \mu\text{W}/\text{cm}^2$ [20, 25, 26]. Given such low offered ambient power density, it is a bend how rectenna can capture as much power as mush power as possible.

In this work a rectenna-grid scheme is used in order to provide the load with enhanced power for low-power density. The combination point took place at DC-area, simplifying the matching network design process. The proposed rectifier is now connected to a pair of custom designed antennas, eventually forming a rectifying antenna, i.e. a rectenna.

It is noted that the use of rectenna grids operating on the same frequency is not new [15, 16]. In contrast to prior art designs, our goal was to fabricate a low-cost rectenna grid which operates adequately, in terms of efficiency and offered power at load, for low power density and power input. The RF-to-DC efficiency was measured according to a specific procedure which took into account the rectenna radiation pattern and utilizes a signal generator, a spectrum analyzer and a calibrated antenna.

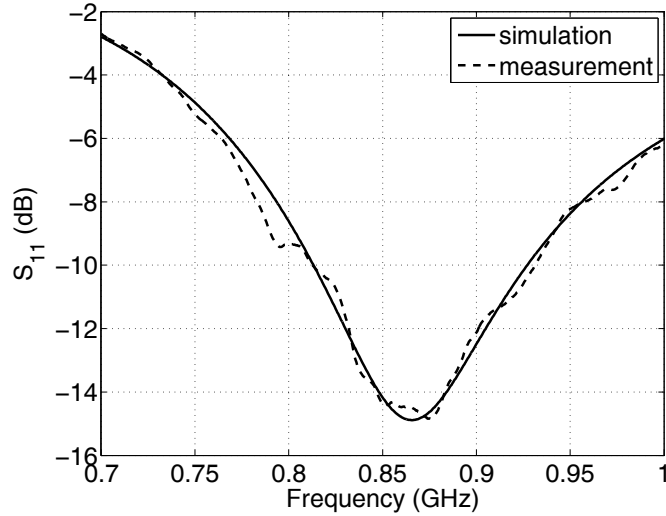


Figure 2.8: Reflection coefficient of the bow-tie antenna.

2.3.1 Rectenna Design and Radiation Pattern

A bow-tie antenna was designed by Stylianos D. Assimonis, to operate at ISM band (around 868 MHz) and the simulated/measured reflection coefficient is depicted in Fig. 2.8. The design is an enhanced variation of a dipole antenna in terms of wide-band operation and low fabrication complexity. The rectifier is accompanied by two such identical bow-tie antennas, forming a rectenna device (Fig. 2.9) with dimensions $10.5 \times 12 \times 5.5 \text{ cm}^3$ (or $0.3\lambda \times 0.35\lambda \times 0.16\lambda$). Due to the closely-spaced, vertical polarized antennas and the proximity with rectifier, the total rectenna radiation pattern is not omni-directional and should be estimated. For far-field simulation, Ansys HFSS was used. Especially, the whole geometry was analyzed at 868 MHz when only one antenna was radiated and the other, with the rectifier, acted as parasitic elements. The simulated far-field in terms of realized gain is depicted in Fig. 2.10 and it is evident that the rectenna is directional, as expected. More specifically, a maximum gain, $G = 4.4 \text{ dB}$ is achieved at horizontal plane, in front of each bow-tie antenna ($\phi = 0^\circ$, $\theta = 90^\circ$). It is noted that there is a plane symmetry at $x = 0$. Hence, the use of two antennas (i.e. rectenna-grid) provide the load with enhanced power for low-power density, while the proximity between the same polarized antennas and the rectifier increases

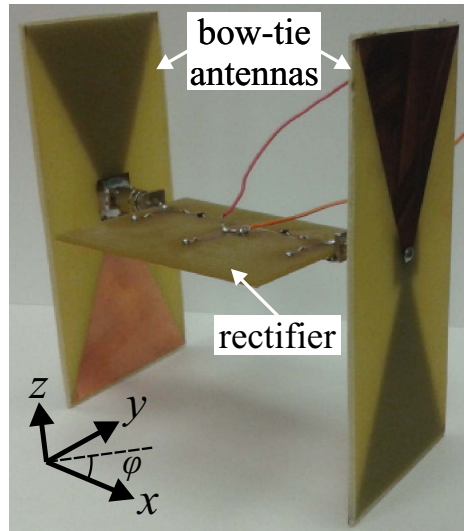


Figure 2.9: The proposed rectenna-grid consisting of two identical bow-tie antennas.

the ability to harvest power from specific directions (directional rectennas).

2.3.2 Rectenna Efficiency

Using 2.7 as rectenna RF-to-DC efficiency is not straight forward since the rectenna does not have a 50Ω ports where measurement of the received RF power is possible. For that reason an estimation of the incident RF power at the measurement plane is required. Different approaches are available: (a) using an antenna with the same geometry, matching it to 50Ω and measuring the received power at each power density; (b) using the antenna effective area obtained from simulation and multiplying with the power density at the plane of measurement; and, (c) using the geometrical area of the antenna and multiplying by the power density. Methods (a) and (b) could raise inaccuracies in the efficiency calculation because the rectifier connected to the antenna is non-linear and loads the antenna differently according to the biasing conditions and power, hence, the amount of RF power received and reflected will change. This could lead to an under estimate of available RF power while would in turn appear as an increase in efficiency. Using approximation (c), P_{in} in 2.7 is calculated as an over estimate. Since this assumes

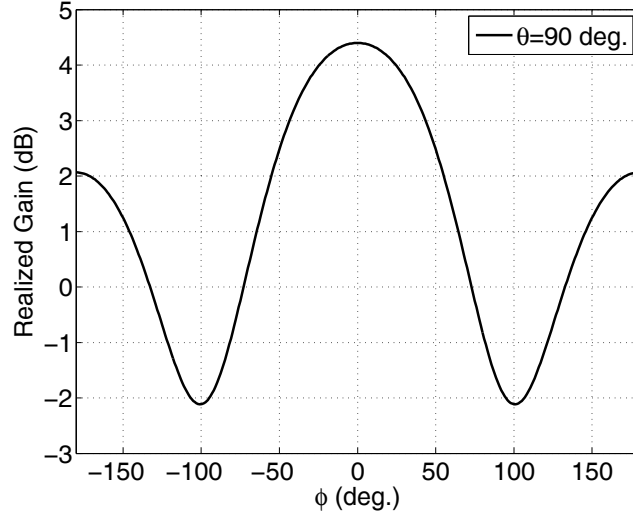


Figure 2.10: The estimated rectenna realized gain. Only one antenna was radiated and the other, with the rectifier, acted as parasitic elements.

that the antenna is 100 % efficient it always leads to an under estimate of efficiency:

$$\eta = \frac{P_{out}}{P_{in}} = \frac{V_R^2/R}{S \cdot A_{eff}}, \quad (2.8)$$

where S is the power density of the incident to the rectenna plane wave and A_{eff} the total antenna effective area:

$$A_{eff} = \frac{\lambda^2}{4\pi} G, \quad (2.9)$$

where λ is the wave length and G the antenna gain.

Fig. 2.11 shows schematically the terms S , A_{eff} , P_{in} and P_{out} . The total RF power P_{in} , to be transformed to DC by the rectifier, is the sum of the power which is captured by the two antennas. It is clear that when the antenna gain is increased, will also increased the A_{eff} and finally the captured power since $P_{in} = SA_{eff}$. The same result can be obtained by increasing the number of the antennas, hence the idea which is presented here could be expanded and applied in $n \times 1$ rectenna grids, where $n \geq 2$. According to (2.9), the effective rectenna area from the both antennas, $A_{eff} = A_{eff,1} + A_{eff,2}$, is equal to 522.86 cm².

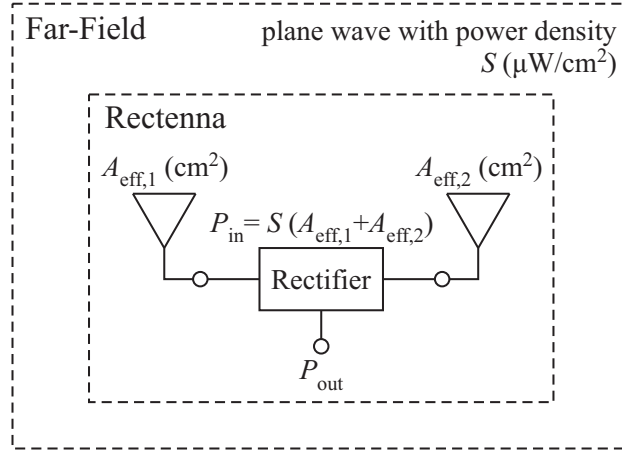


Figure 2.11: Rectenna topology at far-field.

Next, the RF-to-DC efficiency was estimated: A log-periodic antenna, connected to a signal generator was the transmitter. At a specific point in the far-field area, one commercial and calibrated monopole antenna with gain $G_{\text{cal}} = 1.8$ dBi was placed, and connected to a spectrum analyzer, measuring the received power, P_{cal} . The power density S , is estimated from,

$$S = \frac{4\pi}{\lambda^2} \frac{P_{\text{cal}}}{G_{\text{cal}}}. \quad (2.10)$$

Afterwards, the spectrum analyzer and monopole antenna was removed and the proposed rectenna was placed at exactly the same point. Now, the voltage across the load was measured. The RF-to-DC efficiency is depicted in Fig. 2.12. Firstly, it is observed that the rectenna and the rectifier efficiency, measured with different procedures, agree well. The slight difference is mainly due to the estimation via simulation of G . Especially for the rectenna, for $P_{\text{in}} = -20$ dBm efficiency of 20.5 % is achieved, while for -10 dBm efficiency of 35.3 %. Fig. 2.13 shows the measured voltage across the $5 \text{ k}\Omega$ load. For $P_{\text{in}} = -20$ dBm, voltage of 110 mV across the load is measured, while for -10 dBm voltage is equal to 450.5 mV. It is noted that load was fixed to $5 \text{ k}\Omega$.

Fig. 2.14 depicts the rectenna efficiency versus the ambient power density S , of the incident plane wave. For $S = 1 \mu\text{W}/\text{cm}^2$ the efficiency is about

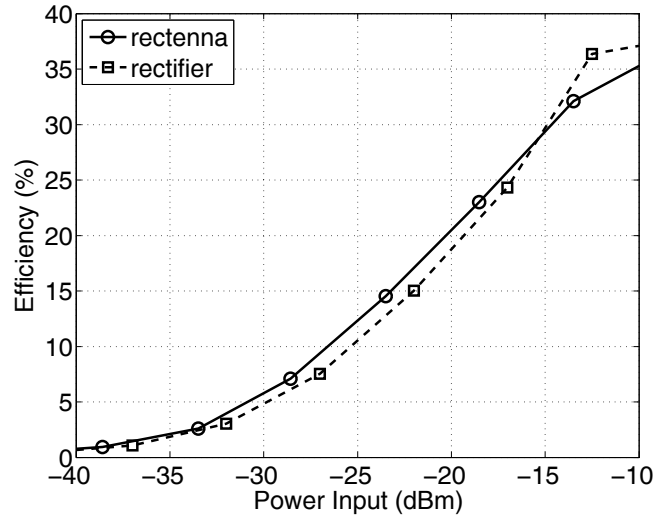


Figure 2.12: Rectenna measured efficiency.

40 %. For $0.01 \mu\text{W}/\text{cm}^2$ efficiency is 15.7 %. Similar conclusions are drawn when the offered power at the load versus power density is studied. Fig. 2.15 depicts the results: a rectenna offers $200 \mu\text{W}$ to load when it is placed in space with power density equal to $1 \mu\text{W}/\text{cm}^2$. For extra low power density $0.01 \mu\text{W}/\text{cm}^2$, the rectenna offers at load $0.8 \mu\text{W}$.

2.3.3 The DC-to-DC Converter

In this section, a DC-to-DC converter is fabricated and used in order to enhance the output voltage of the RF-to-DC rectifier. Specifically, the converter design is inspired from the classical Armstrong oscillator topology and was presented in [36]. It is an autonomous low-voltage and ultra-low power converter. In addition to its self-powering capability (neither external energy source nor external control are needed), this converter was optimized in order to accept very high source impedance (up to several $\text{k}\Omega$). The converter topology is presented in Fig2.16.

This converter contains three blocks (oscillator, voltage stepping-up and the rectifier) which are essentials for its well-functioning. The oscillator is composed by the JFET which amplifies the gates input signal. The oscil-

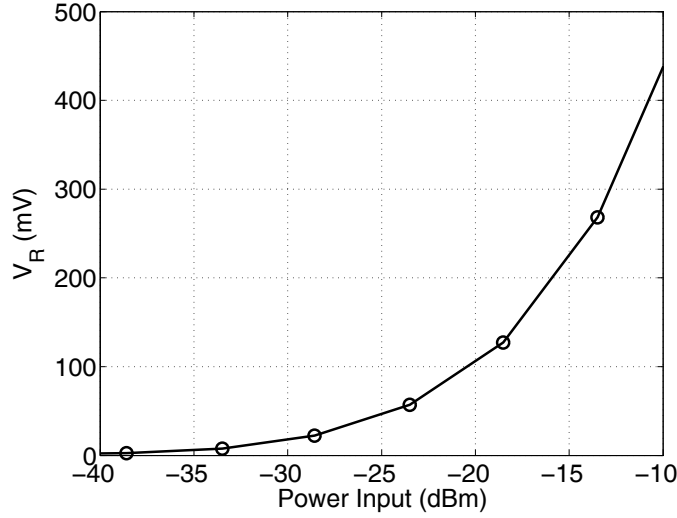


Figure 2.13: Measured voltage across the 5 k Ω load.

lator return loop is formed by the two coupled-inductors and by the gate-source capacitor C_{gs} (which includes main parasitic capacitors). About voltage stepping-up, standard over 1 V level is obtained from a very low source voltage level (some hundreds of mV) via a high step-up ratio transformer. The rectifier: in order to rectify JFET's gate oscillating voltage, the gate-source PN junction of the transistor is used. When the voltage of the gate becomes superior to the diode threshold voltage, the diode is turned ON and the circuit supplies the output load.

When the converter is connected to energy source, the current increases in the primary winding; the secondary winding applies then a positive voltage on the normally-on N- channel JFET's gate. The gate-source PN junction of the JFET is conducting, and the output capacitor is charged with a negative voltage. The output voltage is therefore negative. When the primary current reaches saturation, the voltage across the primary winding cancels and the negative voltage of the output capacitor is applied on the gate of the JFET pinching it off. The current in the primary winding decreases and a negative voltage is applied by the secondary winding on the gate of the JFET, which leads to its switching off. This peak voltage that switched off the JFET falls back to zero and the oscillation process starts again. For the circuit is used

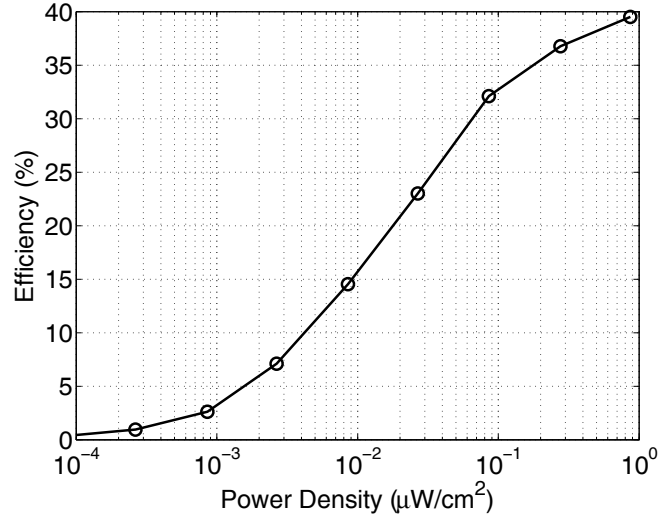


Figure 2.14: Efficiency versus ambient power density.

the transformer 1 : 20 (Coilcraft “LPR6235-253PMB”) and the “BF861A” N-channel JFET. The oscillations start-up conditions satisfied due to the low gate-source cut-off voltage (V_p) and low drain current (I_{DSS}) of the “BF861A” component.

Fig. 2.17 depicts the fabricated RF-to-DC rectifier and the DC-to-DC converter. The rectenna is placed at a specific distance from signal generator in order to achieve P_{in} equal to -20 dBm. The $5\text{ k}\Omega$ is removed and the DC-to-DC converter is connected through cables. The open voltage at the output of the rectifier and the converter is now 298 mV and 1.4 V , respectively. Finally, a 1 mF electrolytic capacitor is connected at the output of the converter. and is measured the total charging time. After about 37 minutes the voltage across the capacitor is increased from 0 to 1.4 V and 0.98 mJ was stored. Assuming a wireless with rate 1 kbps , power consumption 20 mW and 20 bits length-packet, the required energy per packet is equal to 0.4 mJ , hence, the stored energy is capable to supply the sensors nodes of this network.

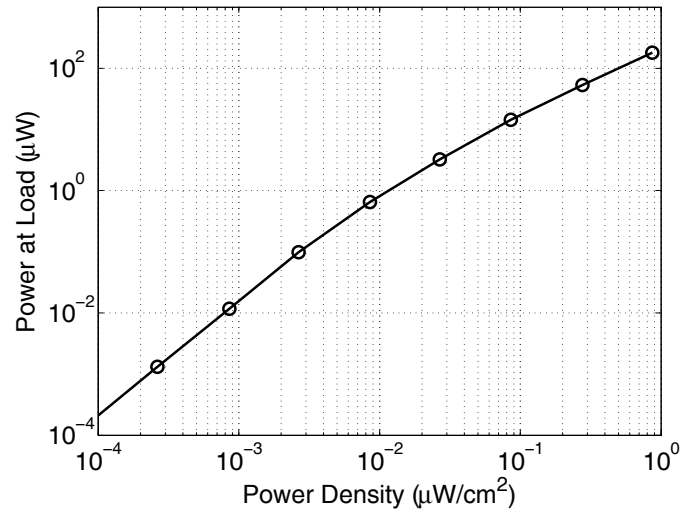


Figure 2.15: The power at the load versus ambient power density.

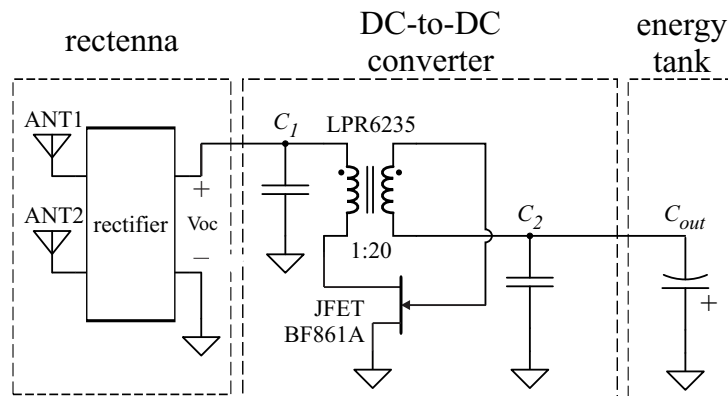


Figure 2.16: Autonomous low-voltage and ultra-low power converter schematic with $C_1 = C_2 = 1 \text{ nF}$ and $C_{out} = 1 \text{ mF}$.

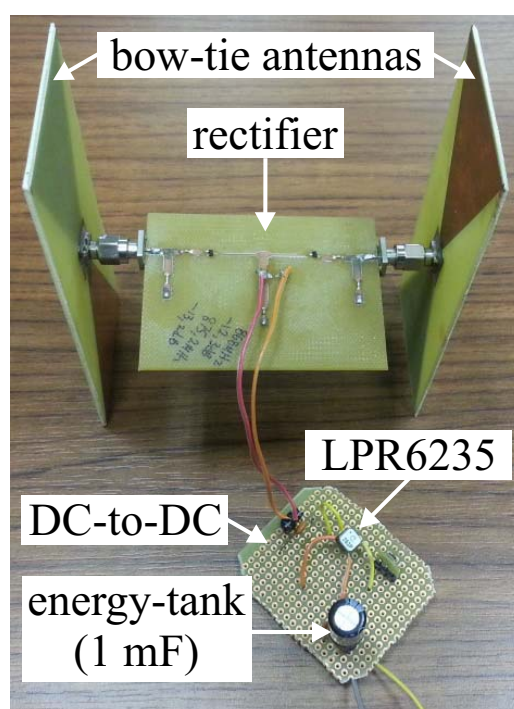


Figure 2.17: The fabricated rectenna and the DC-to-DC converter.

Chapter 3

Sensing for Scatter Radio Tag

3.1 Scatter Radio Communication

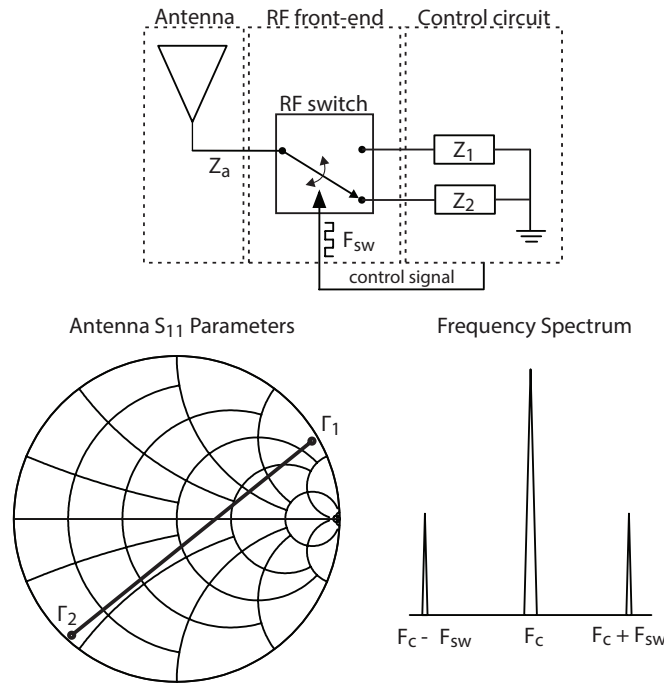


Figure 3.1: Scatter radio communication principles: The low power RF switch alternates the termination loads (Z_1 and Z_2) of the antenna with frequency F_{sw} . When a carrier is equal with frequency F_c , two sub-carriers appear, with frequencies $F_c \pm F_{sw}$.

Scatter radio communication is known from 1948 [37] and today, is exploited in the RFID tags largely. RFID tags are small, low-cost devices that are mainly utilized in object identification. Analog backscatter radio is implemented with an antenna, a control circuit and the radio frequency (RF) front-end between them (Fig. 3.1). The control circuit alternates with a specific frequency, F_{sw} , the termination load of the antenna through a signal

which controls the RF switcher. The latter is located at the RF front-end area. The different termination loads, Z_1 and Z_2 , offer different reflection coefficient, Γ_1 and Γ_2 , respectively, according to,

$$\Gamma_i = \frac{Z_i - Z_a^*}{Z_i + Z_a^*}, \quad (3.1)$$

with $i = 1, 2$, Z_a the antenna impedance. Two typical reflection coefficients are depicted in Fig. 3.1 (down, left). Hence, when a signal with carrier frequency, F_c , impinges on the tag, frequency modulation (FM) occurs and the reflected signal on frequency domain is depicted in Fig. 3.1 (down, right). Finally, the obtained subcarriers are:

$$F_{\text{sub},1} = F_c + F_{\text{sw}}, \quad (3.2)$$

$$F_{\text{sub},2} = F_c - F_{\text{sw}}. \quad (3.3)$$

Different F_{sw} leads to different $F_{\text{sub},i}$. On the other hand, the F_{sw} can be affected by the soil moisture with a specific way, which will be explained below.

3.2 Scatter Radio Sensing Topology

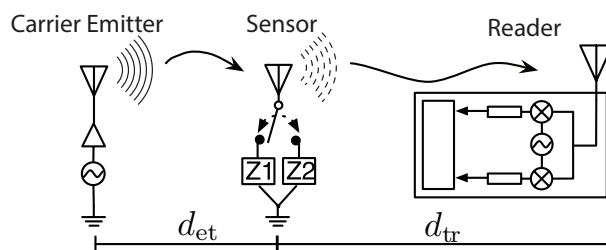


Figure 3.2: Bistatic backscatter sensor network architecture. Low-cost emitter produce the carrier signal which is modulated by sensor nodes and finally, the reflected signal is received by a software defined radio (SDR) reader.

Classic battery-less RFID systems utilize monostatic architectures (i.e., reader in the same box as the carrier emitter) and incorporate high bitrate schemes that greatly reduce the communication range down to a few meters

[38]. On the other hand, environmental monitoring WSNs do not require either battery-less setups or high bitrates, since environmental variables, such as soil moisture and plant signals, change with a slow rate.

In order to increase the communication range with roundtrip path losses reduction, the bi-static scatter radio topology was implemented [39–41], as shown in Fig. 3.2. The carrier emitter, which was a portable simple pulse generator with an amplifier, was placed in a different location from the reader, which was a commercial software defined radio (SDR). The emitter-to-tag and tag-to-reader distance is d_{et} and d_{tr} , respectively (Fig. 3.2).

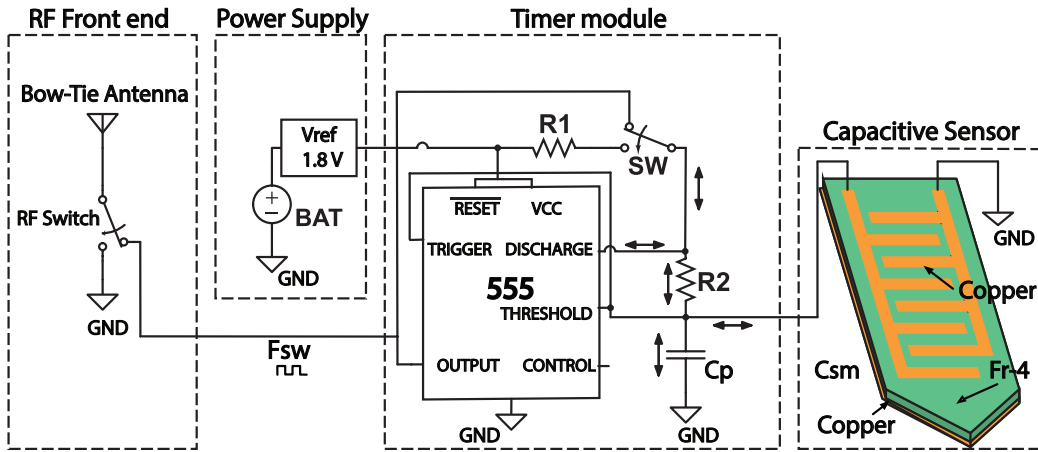


Figure 3.3: Sensor schematic diagram with scatter radio: capacitance varies the timer output frequency, producing a variable-frequency pulse that controls a RF switch; the latter is directly connected to the antenna. [42, 43].

The tag is a low-power, low-complexity and low-cost, analog device. According to the Fig. 3.3, the tag consists of the RF front-end, the power supply part, the timer module and the sensor (capacitive soil moisture sensor). The tag in bistatic topology, scatters soil moisture percentage (%SM) using analog, frequency modulation (FM) at ranges on the order of 100 meters. This manuscript describes the proposed tag system, including a indoor testbed at the end.

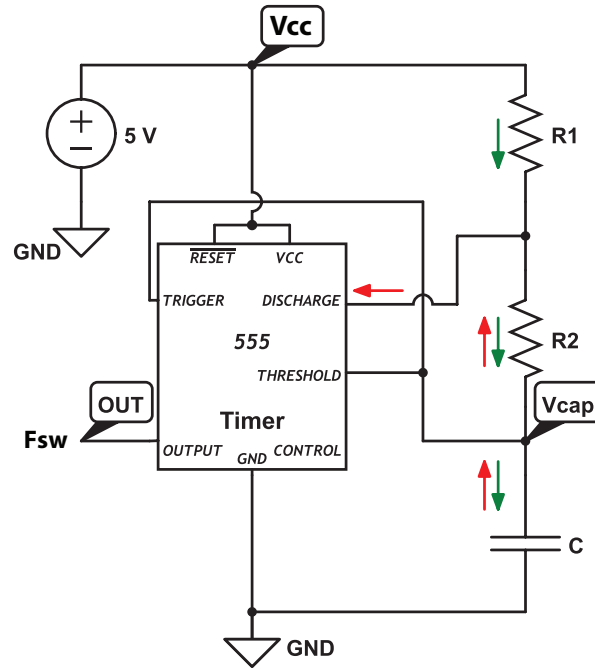


Figure 3.4: The astable multivibrator circuit with 5 V power supply.

3.3 Analog Frequency Modulator

The purpose of the sensor node is to produce voltage pulses of frequency that depends on the %SM and use these pulses to control the rate with which the antenna termination loads are alternated. The soil moisture capacitive sensor converts the soil moisture to capacitance (C_{cm}) then timer module converts the C_{sm} to frequency (F_{sw}) for the RF front-end switching.

An astable multivibrator circuit plays the role of the *capacitance-to-frequency* (CtF) converter. A multivibrator is an electronic circuit (Fig. 3.4) used to implement a variety of simple two-state systems such as oscillators, timers and flip-flops. The name "multivibrator" was initially applied to the free-running oscillator version of the circuit because its output waveform was rich in harmonics. The type of multivibrator that used in this work is the astable, in which the circuit is not stable in either state; it continually switches from one state to the other. It functions as a relaxation oscillator.

The heart of this astable multivibrator circuit is the monolithic timer "CSS555" from Custom Silicon Solutions. The "CSS555" is a micro-power

version of the popular 555 timer IC. It features an operating current under $5 \mu\text{A}$ and a minimum supply voltage of 1.2 V . It actually can be user-programmed to work in various modes, but for the circuit described here, it is used in the standard 555 mode as it comes from the factory. There are four pins that play a critical part in the timer's operation in this mode: "trigger" (TRG), "threshold" (THR), "discharge" (DIS) and "output" (OUT).

At the 555 astable setup, at the start of an ongoing cycle, the timing capacitor C starts charging up through resistors R_1 and R_2 (green arrow at Fig. 3.4); the DIS pin is open and the output pin is "high" (i.e. at the supply voltage V_{cc}). When the rising capacitor voltage reaches the upper trip point, which is $2/3$ of V_{cc} , the OUT and DIS pins go "low", i.e. are connected to ground or 0 V . The capacitor voltage then drops via resistor R_2 (red arrow at Fig. 3.4) until the lower trip voltage, $1/3 V_{cc}$, is reached. This brings the TRG pin to the lower trip voltage and that causes the OUT pin to go "high" again and the DIS pin to disconnect. The cycle then repeats itself as before. Note that the reset pin must be connected "high" for operation; setting this pin "low" stops the timer and the output pin goes "low".

The lengths of the "high" and "low" periods are determined by the values of R_1 , R_2 and C . The "high" time is inherently longer than "low" because the resistance for charging the capacitor is R_1+R_2 , whereas the discharge resistance is just R_2 . The capacitor (C) is periodically charged and discharged through resistors R_1 and R_2 (Fig. 3.3). Thus the frequency F_{sw} and duty cycle which is the ratio of time the output pin is "low" to the total time of a cycle, D of the square wave produced at the output of the astable multivibrator are given by:

$$F_{sw} = \frac{1}{(R_1 + 2R_2)C \ln(2)}, \quad (3.4)$$

$$D = \frac{R_1 + R_2}{R_1 + 2R_2}. \quad (3.5)$$

The diagram below (Fig. 3.5) shows an example how the voltage cycles at the output pin and the timing capacitor (C). The values of the components

were $R_1=100\ \Omega$, $R_2=1\ \text{k}\Omega$, $C=100\ \text{nF}$, $V_{cc}=5\ \text{V}$. After the initial energizing of the circuit, steady state operation is established and the capacitor voltage cycles between $1/3$ and $2/3$ of the supply voltage. On its upward rise, the voltage at the output pin is “high”, V_{cc} ; on its downward discharge, the output voltage is “low”, $0\ \text{V}$.

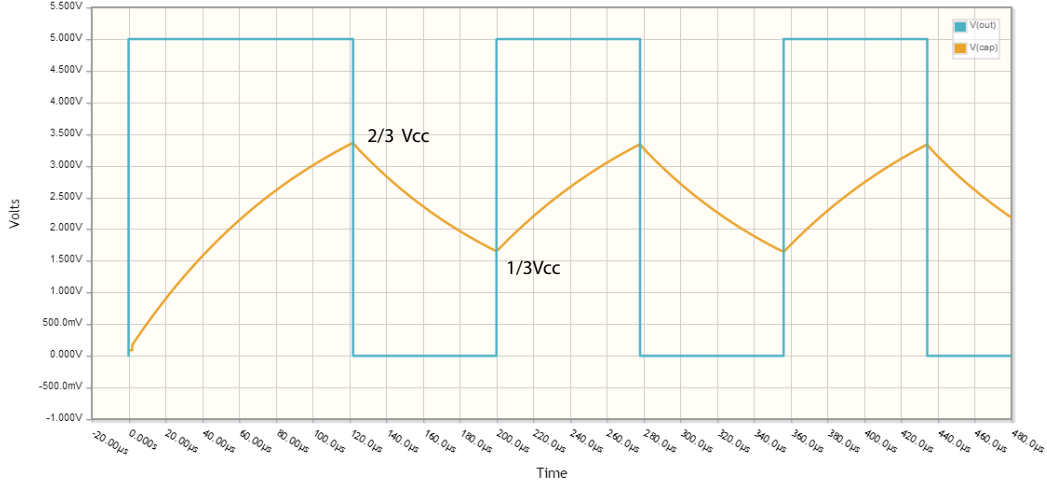


Figure 3.5: Output (blue) voltage and timing capacitor C (yellow) voltage.

In order to adjust the total capacitance range of the tag, capacitor C_p is connected in parallel with the custom sensing capacitor C_{cm} as described in Section 3.5. Thus, the total capacitance C is given by:

$$C = C_p + C_{sm}. \quad (3.6)$$

The tag is supplied from a 3 V lithium-ion battery (type CR2032) and through a voltage reference IC, the timer module operates on input voltage of $V_{cc}=1.8\ \text{V}$ (i.e power supply part in Fig. 3.3). A switch was also placed in the R_1 loop, for power consumption reduction. Now there is not current flow through R_1 while timer output is “low” (see section 3.7).

It is noted that D is always over 50 % since $R1 > 0$. The voltage pulses (F_{sw} in Fig. 3.3) that are produced by the timer module, are driven to the RF switch and, as described in section 3.1, subcarrier (i.e., switching) frequencies are produced when a continuous wave is incident on the antenna. Frequency

modulation of the %SM is implemented, since the value of the subcarrier frequency depends on the value of %SM.

3.4 RF Front-End

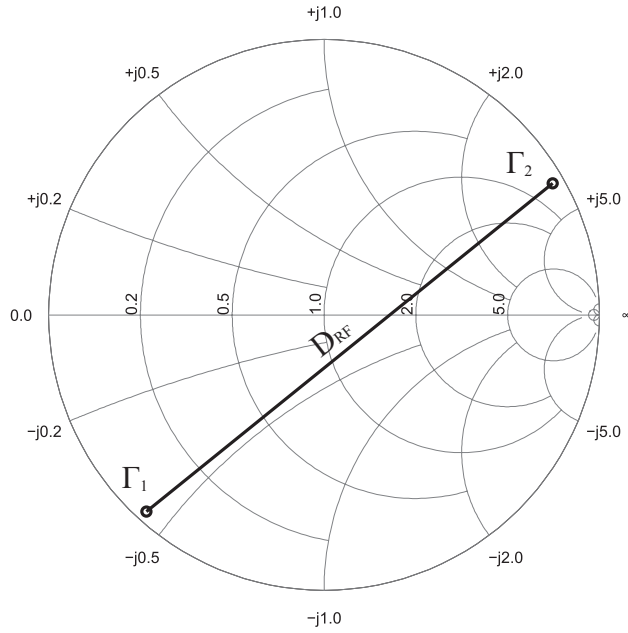
3.4.1 Analysis

The RF front-end (RF front-end in Fig. 3.3) is the part of tag which is responsible for the scattering and therefore its operation is crucial for the communication efficiency of the semi-passive tags. The main purpose of the RF front-end is to maximize scatter radio performance. It consists of an RF switch, an antenna and a control signal (CTRL). The modulation of the scatter signal, (fig. 3.1 up) is performed by the RF switch and its control signal comes from the output of the timer module part (F_{sw}).

The RF switch “ADG919” from Analog Devices was chosen due to its low insertion loss (0.8 dB at 1 GHz) and high isolation (43 dB at 1 GHz). It can be operated from 1.65 V to 2.75 V power supply voltage and its cost is 2.08 €. The switch operates between two states; open circuit and short circuit. For each state i , the antenna terminals have a value Z_i (different loads Z_1, Z_2 in fig. 3.1 up) and the antenna-tag system has a corresponding reflection coefficient Γ_i . The latter describes relation of the amplitude of the reflected wave relative to that of the incident wave and it can be depicted on the Smith chart (as in Fig. 3.6). The reflection coefficient Γ_i of the tag-antenna system for the i -th state of the switch is given by 3.1. Hence, the amplitude of the complex reflection coefficient difference between the two states, or equivalently between two loads, Z_1, Z_2 , connected to the antenna is,

$$D_{RF} = |\Gamma_1 - \Gamma_2|. \quad (3.7)$$

Scatter efficiency is largely dependent on the term D_{RF} which, in the ideal case, when Γ_i s are diametrically opposite on the Smith chart, equals to 2. As D_{RF} increases, scatter performance is improved [44] and therefore it is desired to develop an RF front-end that amounts for a value of D_{RF}

Figure 3.6: Γ_i s on the Smith chart.

that is as close to 2 as possible. However, due to losses and phase that is introduced by the non-idealities of the switch and the printed circuit board (PCB) layout, $D_{RF} = 2$ is not easily achieved.

3.4.2 Design and Fabrication

The design and the fabrication of the RF front-end was based on the [30] in order to select Z_i s such that Γ_i s are diametrically opposite on the Smith chart and maximize the communication efficiency. A separate from the sensor and the timer module, wave-guide structure was fabricated using the CadSoft EAGLE PCB design software (Fig. 4.5, 4.6, 3.7). The structure is connected with three cables with the timer module. The first cable is the GND, the second is the CTRL signal (i.e. voltage pulses F_{sw} in Fig. 3.3) that are produced by the timer module and the third is the power supply voltage.

In Fig. 3.7 can be seen that the switch, is placed very close to the antenna, at the end of the RF front-end geometry in order to avoid introducing phase difference. The mutual coupling reduction, on the RF front-end, is achieved due to the vias near the sma connector and the physical dimensions of the

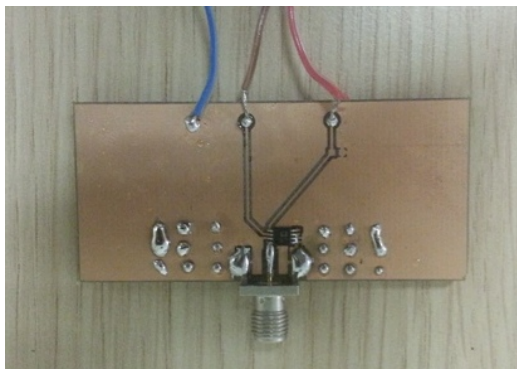


Figure 3.7: Front-end coplanar waveguide structure.

structure.

Experimentation with the specific front-end indicated that $Z_1 = 3.5 - 56.5i$ and $Z_2 = -1.2 + 57.5i$, for -20 dBm power input at 868 MHz. Assuming $Z_a = 50 \Omega$ for antenna load, $D_{RF} = 1.944$ which is a highly improved result near to 2. It is obvious that scatter radio performance is improved in terms of D_{RF} which will in turn lead to improved communication performance.

3.5 Soil Moisture Sensor

This work is aimed at developing wireless sensors for the preventive and proactive management in agriculture, including real-time crop monitoring, analysis and proactive and preventive care solutions for crops. Crop data gathered using wireless precision sensors such as soil moisture sensors would have significant application particularly to measure the by mass water content of the soil in a certain plot of land. This work serves the purpose of presenting the development of a wireless soil moisture sensor which has high sensitivity, robust and low cost with potential for commercialization. Fringing electric and magnetic field sensors are widely used for non-destructive measurements of material properties. This general principle allows design of sensors for a very broad spectrum of applications including relating changes in electrical properties to physical properties such as temperature, density, defects, moisture etc [45]. The performance of fringing electric field (FEF) sensors is typically evaluated based on their penetration depth, signal strength,

measurement sensitivity and linearity. All of these factors depend on sensor geometry [46]. Since 1960s, a number of theoretical and experimental investigations have contributed to different aspects of FEF technology including electric field modelling, industrial and scientific applications, design optimization, and parameter estimation [47]. The soil moisture percentage (%SM) accurate measurements are important to land activities, especially those involving agriculture, forestry, hydrology, and engineering. The variation of soil dielectric constant leads to a change in the capacitance values, which can be captured with proper circuit design. The objective of the sensor design is we want it to be small and affordable, able to do remote monitoring (wireless), durable, robust in the field and easy to deploy. In this section, the FEF soil moisture sensor out of a printed circuit board as a capacitive based sensor is presented.

3.5.1 Theory

There are many popular projects about plant care automation in the electronics community. Recent examples include the “Garduino system”, and the “twitter-enabled Botanicalls”. Both of these systems rely on the fact that the resistance of soil that contains water is lower than the resistance of soil that contains less water. This works, but it has two important drawbacks.

First of all, the electrodes suffer from degradation due to oxidation. The voltage applied to the electrodes in the soil attracts oppositely-charged ions present in the soil or water. These ions then deposit on the surface of the electrode. These oxides are insulators, leading an increasing resistance of the electrodes over time. Second, water is actually a rather poor conductor compared to the impurities it contains. Soil resistance is therefore dependent upon the contamination in the soil more than the moisture content. This means that resistive methods require a calibration step that depends on the soil composition.

According to another idea, soil moisture content may be determined via its effect on dielectric constant by measuring the capacitance between two electrodes implanted in the soil. Where soil moisture is predominantly in

the form of free water, the dielectric constant is directly proportional to the moisture content. A FEF sensor can be visualized as a parallel plate capacitor, whose electrodes open up to provide a one-sided access to material under test. The basic idea of FEF sensing is to apply a spatially periodic electrical potential to the surface of the soil. The combination of signals produced by variation of the spatial period of the inter-digital electrodes combined with the variation of electrical excitation frequency potentially provides extensive information about the spatial profiles and dielectric spectroscopy of the soil.

The capacitor sensor consists of two copper electrodes mounted on the circuit board at some distance (see below) from the top of the head. These electrodes form the plates of the capacitor with the soil, acting as the dielectric in between. The plates are connected to an oscillator, consisting of the astable multivibrator circuit (CtF converter 3.3). The oscillating electric field is generated between the two plates and extends into the soil medium through the wall of the sensor. Changes in dielectric constant of surrounding media are detected by changes in the operating frequency. The output of the sensor is the frequency response of the soils capacitance due to its moisture level.

The application for such a device is measuring the water content of soil (%SM), where the volume of water in the total volume of soil most heavily influences the dielectric permittivity of the soil. Dielectric permittivity of water ($E_r=80$) is much greater than the other constituents of the soil (mineral soil: $E_r=4$, organic matter: $E_r=4$). When the amount of water changes in the soil, a probe will measure a change in capacitance due to the change in dielectric permittivity that can be directly correlated with a change in water content.

3.5.2 Sensor Design

According to Fig. 3.8, alternate current signal is supplied to the driven electrodes -1- and the output signal will be measured from the sensing electrodes -2-. FR4 PCB material is used as the substrate -3- and has height 1.5 mm. The purpose of ground plane electrode -4- is to reduce parasitic capacitance

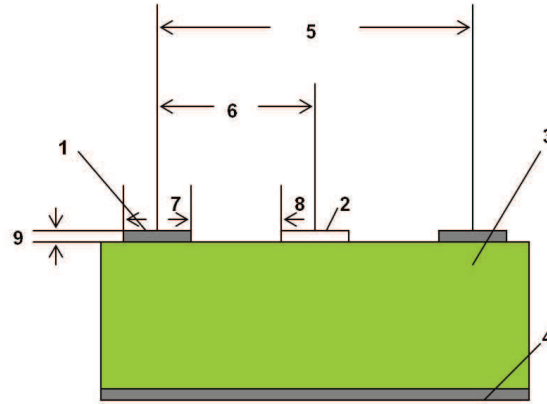


Figure 3.8: Schematic diagram of cross section of FEF soil moisture sensor. [1]

in order to increase sensor sensitivity. Spatial wavelength λ_c -5- is defined as the distance between the centerlines of neighbouring electrodes of the same type. In our design is about 8 mm. Half λ_c (4 mm) is the distance between the centerlines of the adjacent electrode belonging to different electrodes -6- (drive-sense electrode). The electrode width -7- and distance between different electrodes -8- is usually $1/4 \lambda_c$. The thickness of the electrode -9- is made from copper material and it is $0.35 \mu\text{m}$. The sensor device electrode is coated with a certain thickness of insulator (subsection: 3.5.4) to obtain more robust sensor device.

According to (3.6) the soil moisture sensor is represented as a capacitor C_{sm} and as shown in Fig. 3.3 the drive electrode of the sensor is connected to the THR pin of 555 timer. The sense and drive electrodes were placed side by side and the ground plane underneath them is to control the flux distribution (Fig. 3.9). In this work, the finger width was fixed at 2 mm and the finger length was fixed at 18 mm. The sense electrode was connected to the GND of tag and the ground plane was not connected to the sense electrode in order to reduce the overall capacitance of the sensor. The drive electrode is driven by a sinusoidal time varying signal with known amplitude and radian frequency. This signal is the timing capacitor voltage (Fig. 3.5) and its frequency is equivalent with the F_{sw} at the output of the CtF converter. The sense electrode is capacitively loaded. Electric fields originating from the driving electrodes penetrate through the soil and then terminate on the

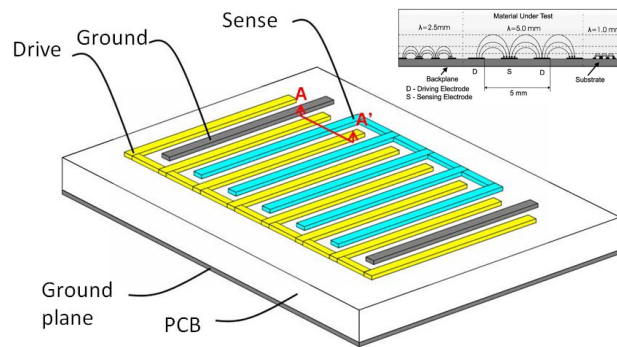


Figure 3.9: Soil moisture sensor schematic diagrams.

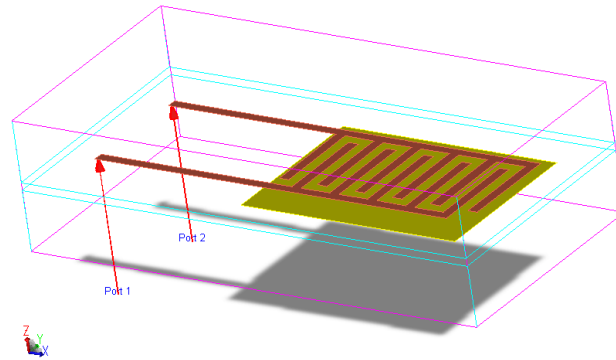


Figure 3.10: ADS 3D Preview of sensors electrodes, the ports are used for model simulation.

sensing electrodes. The dielectric properties of the soil alter the distribution of the field lines.

3.5.3 Simulation

Simulations are conducted using Agilent Technologies ADS software, with the method of moments solver. The quality of the results from moment method depends on model definition as well as mesh generation and the frequency plan. When the right model and mesh are chosen, moments simulations can generate results with high accuracy. For the simulation only the design of sensing area with the GND plane has been analysed, excluding the electronic circuitry effect.

Firstly, a layout design of sensor was created as is depicted in Fig. 3.10,

with parameters: mesh =1 GHz, frequency plan =50 to 100 kHz. The method of moments solver was achieved after that. Two separate cases of simulation related with relative dielectric permittivity of the dielectric were implemented. In one case the sensor was simulated with air as dielectric material ($E_r= 1$) and in the other case was simulated with water as dielectric material ($E_r= 80$). It is noted that between the sensor and the dielectric has been placed a thin layer of polyester resin as insulation (see below) with $E_r= 4$.

In order to be calculated the capacitance of sensor from the method of moments, were exported the scattering matrix (S parameters), the admittance matrix (Y parameters) and the impedance matrix (Z parameters). The effective capacitance C_1 , C_2 , C_3 in pF was calculated by,

$$C_1 = \frac{-e^{12}}{2\pi F * \text{imag}(\frac{1}{Y_{1,1}})}, \quad (3.8)$$

$$C_2 = \frac{e^{12}}{2\pi F * \text{imag}(\frac{1}{Y_{2,1}})}, \quad (3.9)$$

$$C_3 = \frac{-e^{12}}{2\pi F * \text{imag}(\frac{(Z_{1,1}Z_{2,2})-(Z_{1,2}Z_{2,1})}{Z_{2,1}})}. \quad (3.10)$$

Fig. 3.11 shows the capacitance value of C3 (3.10) from two different simulation cases (air and water) versus the number of sensor fingers. The capacitance value is increased when the number of fingers are increased. There is no ground electrode and this shows that the increment of finger number do influence the capacitance value of the moisture sensor. Thus, the sensitivity of the sensor will be increased.

3.5.4 Fabrication and Insulation

After the simulation the design with six drive fingers (11 fingers) was selected in order to reduce the capacitance of the sensor.

The sensor was fabricated using the lab's "CNC" milling machine and

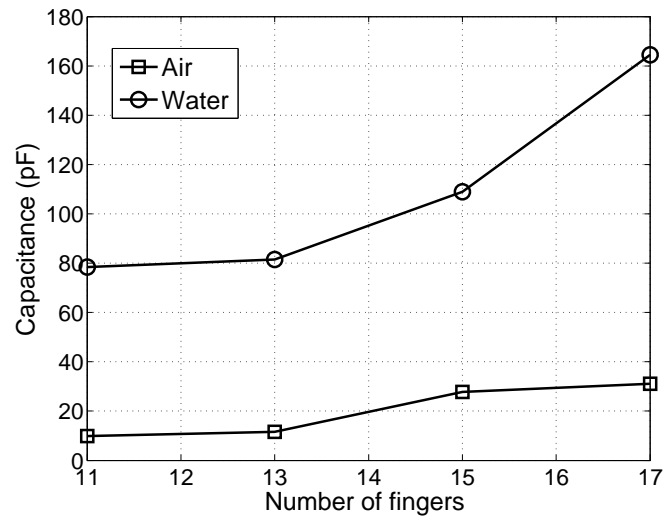


Figure 3.11: Capacitance(pf) vs Number of drive fingers.

in order for the fingers to be really waterproof, four types of isolation were tested. During the work, the PCB solder mask, the plastic tape, the PCB coating spray and the polyester resin material were tested (Fig. 3.12).

To make sure that the different types of isolation on the sensor was really waterproof, an extended soak test was performed. In order to be usable the sensor needs to have a resistance that is at least an order of magnitude larger than the discharge resistor in the measuring system, even after being submerged for a significant period of time. The sensor is designed with a resistor in the mega-ohm range. The resistance needs to remain above 10 M Ω or so. After 12 hours in a glass of water, the resistance must be still above the highest range on the multi-meter. After the tests only the polyester material was considered suitable for the sensor insulation and so the other materials were rejected.

3.5.5 Measurements

The sensor after the installation of insulation was connected to a reference analog frequency modulation through two coaxial cables with known capacitance per meter. The output frequency was measured in the air and in a the glass of water and through the (3.4) and (3.6) was calculated the final

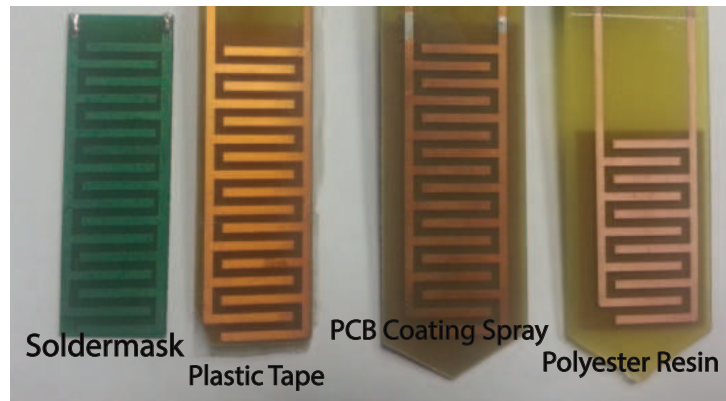


Figure 3.12: Fabricated sensors with different types of insulation.

capacitance of the sensor, C_{sm} . The theoretical results with the experimental had a deviation of the order of 3 pF. According to sections 3.9 and 3.11 the sensor was placed together with the rest of the circuit in a single board and was calibrated in a soil sample at 7 cm depth.

3.6 Plant Signal Sensor

3.6.1 Analysis

The electrical signals generated by plants are associated with their health status, as well as the corresponding environmental conditions (e.g. water deficit, temperature, pollination, wounding etc.) [48], [49]. These studies have shown that plants respond rapidly to external stimuli by producing electrical signals through the animal-like neural system that they enclose.

Slow wave potentials (VP) and rapid propagated potentials (AP) are two types of electrical signals that are associated with pollination, watering, temperature changes, wounding and mechanical stress [50]. Other studies indicate specific avocado electrical signals that denote severe water deficit condition in avocado trees, [51] and [52].

The existing studies that are associated with the investigation of the plant signalling have been conducted with special equipment that doesn't offer a wide scale testbed of the plant signalling that provides in the same time a

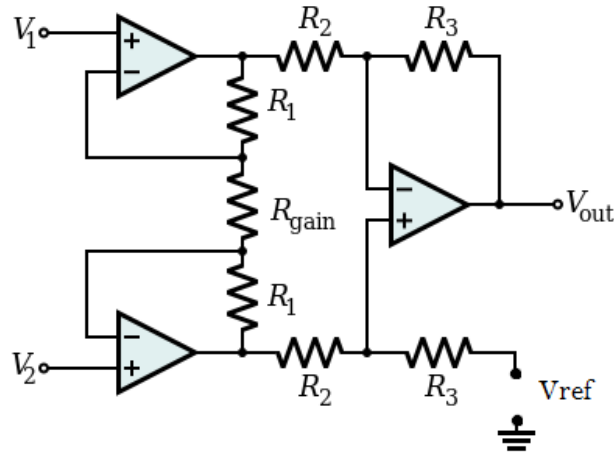


Figure 3.13: Instrumentation amplifier schematic.

low cost sensor per plant. Specifically, desktop exquisite laboratory amplifiers and data loggers have been used in order to provide signal condition and data logging operation. At [52] and [51], a laboratory multimeter (“KEITHLEY 2701”) and micro-probe amplifier (“WP M-707”) are deployed, respectively, for signal conditioning. In this work we present the development of special sensor that interfaces the electrical signals that are produced from plants. The signal condition circuit is composed of a low cost instrumentation amplifier. The instrumentation amplifier offers, accuracy, stability and high common rejection rate which eliminates the parasitic common signals of both pairs of electrodes-cables.

In order to provide a wireless sensor for agricultural purposes that a plant can be interfaced by a low cost and low power node, a semi passive backscatter tag powered with voltage circuit oscillator (VCO) will be developed. The Backscatter tag, provided with a low power timer, configured as VCO and the plant signal sensor, will be able in the future, to backscatter the value of the electrical potential back to reader.

3.6.2 Circuit Design

The instrumentation (or instrumentational) amplifier circuit is a type of differential amplifier that has been outfitted with input buffer amplifiers, which

eliminate the need for input impedance matching and thus make the amplifier particularly suitable for use in plants signals measurements. Additional characteristics include very low DC offset, low drift, low noise, high open-loop gain, high common-mode rejection ratio, and high input impedances. The electronic instrumentation amplifier internally composed of 3 operational amplifiers (op-amps) as is depicted in fig. 3.13. These are arranged so that there is one op-amp to buffer each input (+, -), and one to produce the desired output with adequate impedance matching for the function. Furthermore an extra op-amp is used to supply a voltage reference to the circuit. The gain and the output of the circuit is:

$$G = \frac{R_3}{R_2} \left(1 + \frac{2R_1}{R_{\text{gain}}} \right), \quad (3.11)$$

$$V_{\text{out}} = (V_2 - V_1)G + V_{\text{ref}}. \quad (3.12)$$

The rightmost amplifier, along with the resistors labelled R_2 and R_3 is just the standard differential amplifier circuit, with gain = R_3/R_2 and differential input resistance, $2R_2$. The two amplifiers on the left are the buffers. With R_{gain} removed (open circuited), they are simple unity gain buffers; the circuit will work in that state, with gain simply equal to R_3/R_2 and high input impedance because of the buffers. The single resistor R_{gain} between the two inverting inputs is a method that increases the differential-mode gain of the buffer pair while leaving the common-mode gain equal to 1. This increases the common-mode rejection ratio (CMRR) of the circuit and also enables the buffers to handle much larger common-mode signals without clipping than would be the case if they were separate and had the same gain. Another benefit of the method is that it boosts the gain using a single resistor rather than a pair, thus avoiding a resistor-matching problem (although the two R_1 s need to be matched), and very conveniently allowing the gain of the circuit to be changed by changing the value of a single resistor. A potentiometer used for R_{gain} , providing easy changes to the gain of the circuit, without the complexity of having to switch matched pairs of resistors.

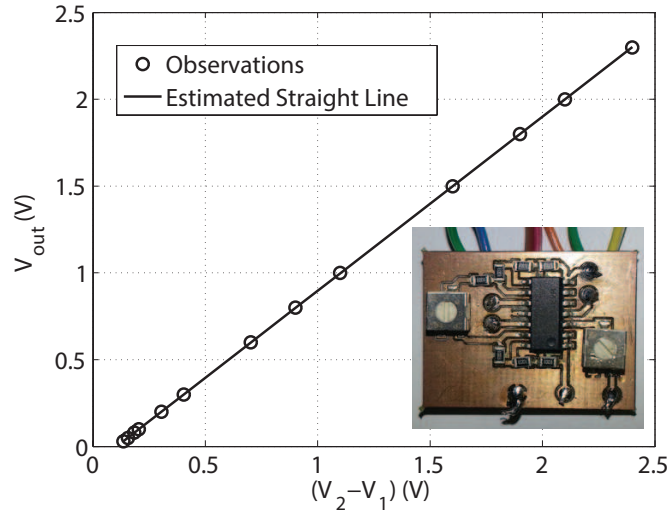


Figure 3.14: Fabricated sensor and calibration characteristic.

The ideal common-mode gain of an instrumentation amplifier is zero. In the circuit shown, common-mode gain is caused by mismatches in the values of the equally numbered resistors and by the mismatch in common mode gains of the two input op-amps.

In the circuit was used the quad operational amplifier “MCP6044” by MICROCHIP. It is low cost (1.2 €) with a low typical operating current of 600 nA and an offset voltage, less than 3 mV. Finally the “MCP6044” operates with a single supply voltage that can be as low as 1.4 V.

3.6.3 Fabrication and Measurements

The plant signal sensor circuit design (Fig. 4.1, 4.2) was implemented at Cad-Soft EAGLE PCB design software and was followed the PCB construction at the CNC milling machine. In order to achieve $G = 1$, R_{gain} was removed (open circuit) and the other resistor values were $R_1 = R_2 = R_3 = 100 \text{ k}\Omega$.

After the PCB construction (fig. 3.14 small photo), the sensor was connected to three power supply signals (V_2 , V_1 and V_{ref}) and was measured the output voltage (V_{out}). The sensor was calibrated using the aforementioned procedure (i.e Least Squares Fitting) for $V_{out} = 30 \text{ mV}$ to 2.3 V, with $V_{ref} = 100 \text{ mV}$. Using the characteristic function depicted in fig. 3.14, the results

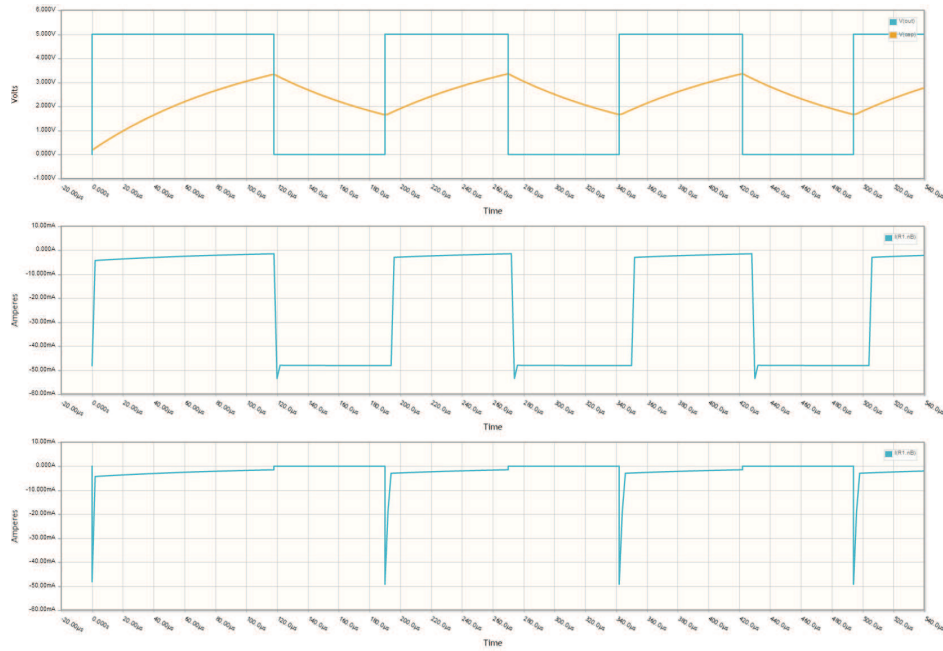


Figure 3.15: Current consumption at R_1 loop with (third graph) and without (second graph) the switch.

were compared to a reference sensor.

3.7 Power Supply

The power supply circuit (power supply in Fig. 3.3) is a crucial part of the tag, since the battery life depends on it. Its purpose is to provide a stable reference voltage to the tag, and to enable the connection of energy harvesting devices. For this purpose, a battery, a voltage reference integrated circuit (IC) and two capacitors have been utilized. The power source of the sensor is a 3 V lithium-ion battery (type “CR2032”). The battery was connected to the input of the voltage reference IC (“REF3318AIDBZT” by Texas Instruments) which provides a stable voltage (V_{cc}) 1.8 V to the timer module. The IC consumes 5 μ A and is utilized to accommodate battery voltage drops.

The total power dissipation of the tag depends on multiple factors and is calculated below:

$$P_{\text{tot}} = P_{\text{ch}} + P_{\text{q}}. \quad (3.13)$$

Each of the variables above denote a factor that consumes power. Particularly, P_{ch} is the average power required for charging the timer capacitors. As observed above is not dissipated power on resistor R_1 and the reason is that has been placed a switch (“SN74LVC1G3157” by Texas Instruments) in the R_1 loop. The switch is closed when timer output is logic “low”, so there is no leakage current through the resistor. The switch (sw) is evident in timer module in Fig. 3.3. In Fig. 3.15 can be seen the current consumption at R_1 loop, with and without the switch (third and second graph) for the example of Fig. 3.5. When the capacitor has been reached at 1/3 of supply voltage, in the third graph is observed an instant peak due to the change of switch status from “OFF” to “ON”.

P_{q} is the quiescent power dissipated by the timer, the voltage reference IC, and the R_1 switch IC. The components that were utilized in the tag design consume a quiescent power $P_{\text{q}} = 17.87 \mu\text{W}$.

As stated above, due to the astable operation of the timer, the total capacitance $C = C_{\text{p}} + C_{\text{SM}}$ is charged from $V_{\text{cc}}/3$ to $2V_{\text{cc}}/3$ in $(R_1 + R_2)C \ln(2)$ seconds. Therefore, since a first-order RC circuit is formed by R_1 , R_2 and C , the voltage $V_{\text{c}}(t)$ which is developed across C and the current $I(t)$, drawn by the power supply, are given by:

$$V_{\text{c}}(t) = V_{\text{cc}}(1 - e^{\frac{-t}{(R_1+R_2)C}}) + V_{\text{c}}(0) e^{\frac{-t}{(R_1+R_2)C}}, \quad (3.14)$$

$$I(t) = \frac{V_{\text{cc}} - V_{\text{c}}(t)}{R_1 + R_2}, \quad (3.15)$$

where $V_{\text{c}}(0) = V_{\text{cc}}/3$ is the initial condition of the capacitor voltage. Thus, using (3.14) and (3.15), the average power P_{ch} drawn by the power source,

V_{cc} , during a period of $1/F$, is calculated as follows:

$$P_{ch} = F \int_0^{(R_1+R_2)C \ln(2)} V_{cc} I(t) dt \quad (3.16)$$

$$= \frac{V_{cc}^2}{3(R_1 + 2R_2) \ln(2)}. \quad (3.17)$$

For example considering a tag with $R_1 = 8.8 \text{ k}\Omega$, $R_2 = 17.6 \text{ k}\Omega$ and $C = 1020 \text{ pF}$ operating at $F_{sw} = 30 \text{ kHz}$ consumes $P_{ch} = 40.74 \text{ }\mu\text{W}$ and $P_q = 17.87 \text{ }\mu\text{W}$ summing the previous $P_{tot} = 58.61 \text{ }\mu\text{W}$. As can be seen from the above calculations the value of R_1 resistor is half the value of R_2 resistor. This is because we have defined the duty cycle (D) to be 60 %. By solving the (3.5) = 0.6 have $R_1 = R_2/2$. It would be ideal as you will see below, have $D = 50 \text{ }\%$.

The duty cycle effects the communication performance since the implemented receiver depends on the power of the *fundamental* subcarrier frequency of the scatter radio signal. The latter is given by [53]:

$$P(a_1) = \left[\frac{A\sqrt{2}}{\pi} \sin(\pi D) \right]^2, \quad (3.18)$$

where A is the peak-to-peak amplitude of the pulse signal. For $D = 50 \text{ }\%$, the $P(a_1)$ is maximized; when the duty cycle is higher (or lower) than 50 %, the power of the fundamental frequency is decreased. Above is an example with tree tags with the same subcarrier frequency of 51 kHz, where one tag has $D = 50 \text{ }\%$ the other has $D = 60 \text{ }\%$ and the last has $D = 75 \text{ }\%$, then the total power consumption and power of their fundamental frequencies are calculated using (3.4), (3.5) and (3.18). The results are presented in Table 3.1. It is observed that all the sensors have the same power consumption due to the switch's position in the R_1 loop. Regarding the power of their fundamental frequencies, the sensor node with $D = 50 \text{ }\%$ has the maximum $P(a_1)$, the second one with $D = 60 \text{ }\%$ has a smaller value $P(a_1)$ than the first. The latter lacks of power in its fundamental frequency by a factor of 1.81, which in turn will result in less accurate reception.

Table 3.1: Example of three tags with different duty cycle D .

| $R_1(\text{k}\Omega)$ | $R_2(\text{k}\Omega)$ | $D(\%)$ | $P_{\text{tot}}(\mu\text{W})$ | $P(a_1)$ |
|-----------------------|-----------------------|---------|-------------------------------|-----------------------|
| 0 | 7.8 | 50 | 132.5 | $(A\sqrt{2})^2/\pi^2$ |
| 3.1 | 6.2 | 60 | 132.5 | $(1.81A^2)/\pi^2$ |
| 7.8 | 3.9 | 75 | 132.5 | A^2/π^2 |

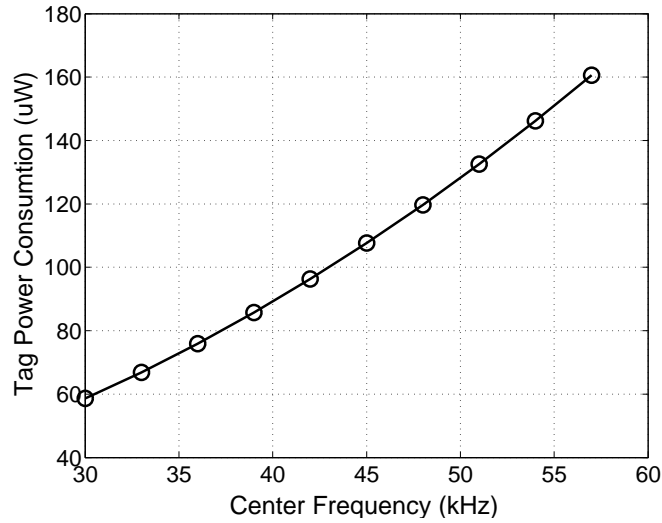


Figure 3.16: Power consumption of ten tags.

In in Fig. 3.16 is presented the power consumption of ten tags that each of these has different center frequency (kHz) and the same $D = 60\%$. It is observed that when the center frequency of tags increased from 30 kHz to 57 kHz, the power consumption also is increased, and the increment is not linear.

Finally according the above example the ultra-low power consumption of 32.5 uA at 1.8 V ($58.61 \mu\text{W}$), provides a lifetime of 12.8 months of continuous (not duty-cycled) operation with the utilization of a 300 mAh “CR2032” battery.

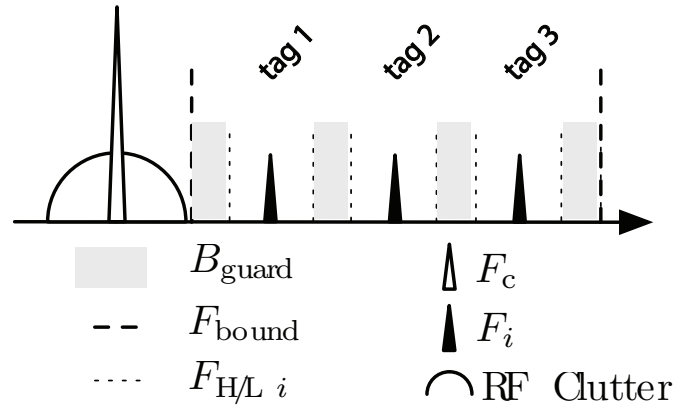


Figure 3.17: Scheme for networking multiple tags. Each tag operates in different frequency bands, while guard bands are set up in between to avoid collision.

3.8 Multiple Access

In this work we constructed four sensor nodes with each of them operating in different center frequency. This WSN employs a multiple access control (MAC) scheme that is responsible for the simultaneous communication of multiple tags with the receiver. As described above, the output frequency (F_{sw}) of the 555 timer module, and as a result, the subcarrier frequency, depends on the %SM value. The frequency division multiple access (FDMA) is adopted which works in a way that every tag is assigned a distinct frequency band for operation, in order to avoid collision [11], [54]. The Fig. 3.17 shows the idea, where can be observed that each tag is allocated a specific frequency band and, also, guard-bands are employed between adjacent sensor-bands.

Many of the above backscatter nodes can operate simultaneously, using FDMA. Fig. 3.18 depicts the obtained subcarriers of four sensor nodes and the carrier at 868 MHz. Frequency shifting of the produced subcarriers is achieved when soil moisture changes from 0 % to 100 %, while, simultaneously, signal collision is avoided. In order to avoid collisions the each sensor has a specific frequency band (bandwidth) and between adjacent sensor-bands there is a guard-band of 1 kHz. In figure are illustrated the subcarriers that corresponding to 0 % SM.

The subcarrier frequency value of each sensor is controlled by the values

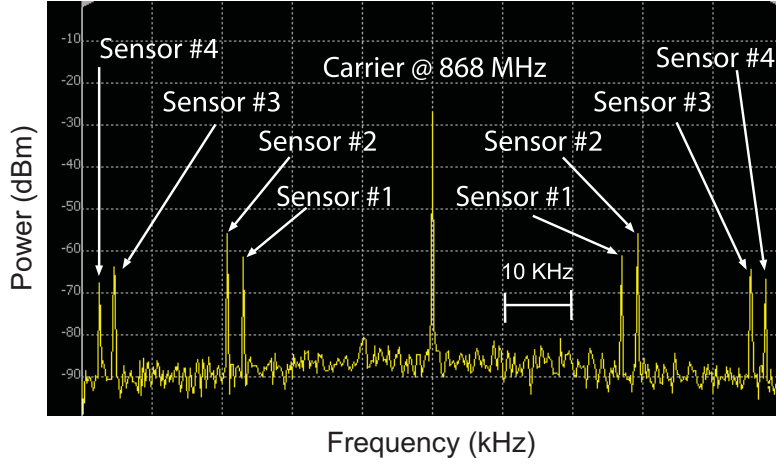


Figure 3.18: Sensor network spectrum for sensors 1, 2, 3, 4. Sensors 1, 2 and 3, 4 occupy a bandwidth of 1 and 5 kHz, respectively.

of resistors and capacitors (R_1, R_2, C) in the RC network that is attached to the timer module. Therefore, the center frequency as well as the total spectrum that each tag occupies can be controlled by selecting components with appropriate values. Specifically, size of the spectrum band that the i -th tag/sensor occupies depends on the lowest and highest frequency that is produced by the timer. Let $F_{sw,i}^L$ and $F_{sw,i}^H$ denote the subcarrier frequency output of the i -th tag. The subcarrier frequency is produced by the timer module when the %SM is 100 and 0, respectively. Then, by using (3.4), the total bandwidth B_i for the i -th tag is calculated follows:

$$\begin{aligned}
 B_i &= F_{Hi} - F_{Li} \\
 &\stackrel{(3.4)(3.6)}{=} \frac{1}{R_i(C_L + C_{pi}) \ln(2)} - \frac{1}{R_i(C_H + C_{pi}) \ln(2)} \\
 &= \frac{C_H - C_L}{\ln(2) R_i (C_L + C_{pi})(C_H + C_{pi})}, \tag{3.19}
 \end{aligned}$$

where $R_i = R_{1i} + 2R_{2i}$ and C_L and C_H are the sensing capacitance values for 0 %SM and 100 %SM, respectively. The $C_{p,i}$ and R_i at i -th node using (3.4)

and (3.19), is :

$$C_{p,i} = \frac{B_i C_L + F_{sw,i}^L (C_H - C_L)}{B_i}, \quad (3.20)$$

$$R_{1,i} = \frac{1}{2} R_{2,i} = \frac{B_i}{3 (\ln(2) F_{sw,i}^L (C_H - C_L) (F_{sw,i}^L + B_i))}. \quad (3.21)$$

The FDMA scheme is implemented, simply with the utilization of specific capacitor and resistor values, based on the calculations above.

During the scatter radio communication, even and odd harmonics are created that can distort the subcarriers of the following tags in frequency band. Fig. 3.19 depicts the subcarriers and harmonics of sensor 1 and sensor 2.

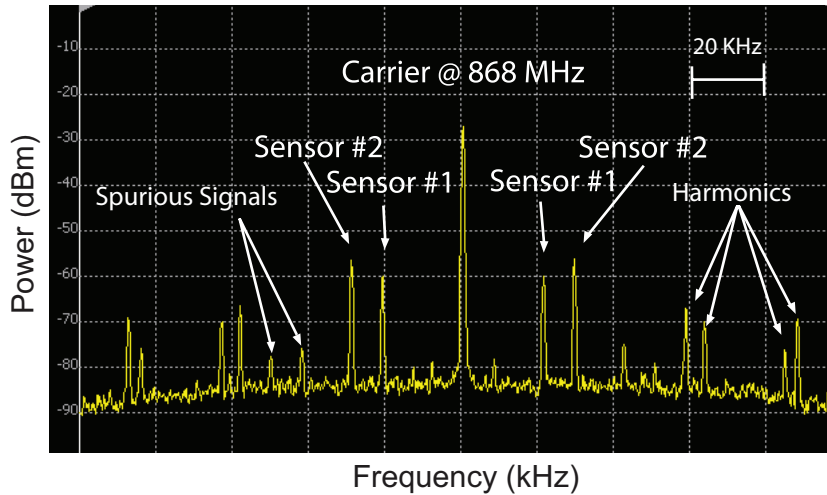


Figure 3.19: Sensor network spectrum for sensors 1, 2. Harmonics and spurious signals are observed.

3.9 Sensor Node Construction

Four nodes were fabricated in-house in order to evaluate the proposed system. The circuit was designed at CadSoft EAGLE PCB design software (Fig. 4.3, 4.4) and followed the PCB construction at the lab's CNC milling machine.

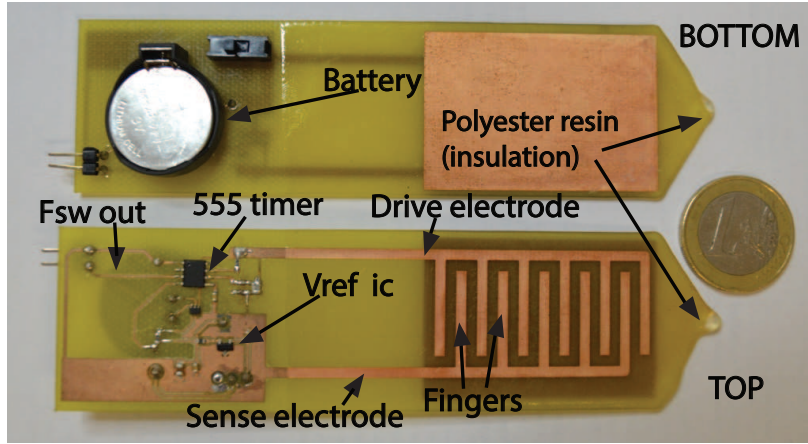


Figure 3.20: Fabricated circuit board with capacitive sensor, power supply circuit and timer module circuit.

In Fig. 3.20 is presented the sensor node including the fabricated microstrip capacitive sensor and its parts as explained in the previous sections. The battery was placed in the back due to lack of space, and the GND plane don't cover the entire surface of the circuit. For completion of the sensor board, was placed a "ON OFF" switch to turn off the power from the battery, and two headers for the output frequency and GND.

At each backscatter sensor node the bow-tie antenna with the RF front-end was located well above the ground, while the fabricated capacitor was placed into the soil. The connection between the switch and the timer was established via shielded coaxial cables (Fig. 3.21).

3.10 Receiver

The receiver utilizes a commodity SDR platform based on homodyne architecture. A periodogram-based, subcarrier frequency \hat{F}_i estimator was implemented for each i -tag:

$$\hat{F}_i = \arg \max_{F \in [F_{iL}, F_{iH}]} |X(F)|^2, \quad (3.22)$$

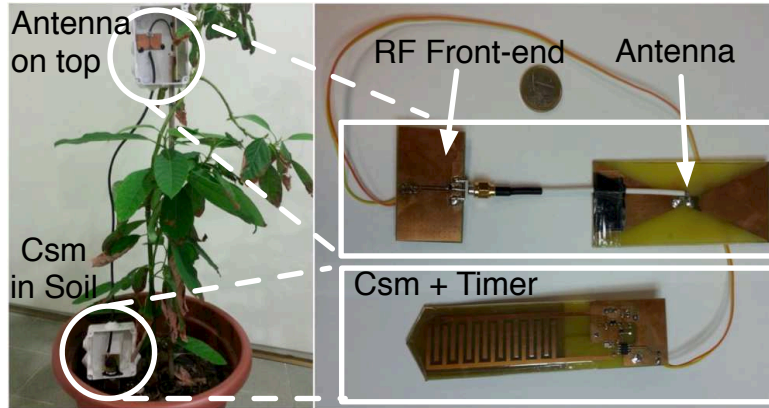


Figure 3.21: Left: Installation of the sensor on an avocado plant with utilization of “IP65”-rated enclosures. Right: Close-up view of the fabricated sensor.

where, $X(F)$ is the Fourier transform of the baseband downconverted and carrier frequency offset (CFO)-compensated signal. CFO estimation and compensation was based on time and frequency domain techniques [55]. F_{Li} and F_{Hi} denote the lowest and highest possible frequency output of the i -th tag, respectively, which are a-priori known. Thus, the frequency component with the maximum power for each spectrum band is estimated as the corresponding sensor’s output frequency.

3.11 Calibration

Calibration is one of the most important procedures that affect the accuracy of sensors. It is the process of calculating the transfer function that converts the output of the sensor to a value of interest. Calibration involves monitoring the nodes’ frequency output for various %SM values and calculating the corresponding transfer function using polynomial fitting. The purpose of this method is to find such polynomial function that its outputs exhibit minimal deviation from the recorded outputs for the corresponding stimuli [56, 57]. The output of the device under calibration is monitored for stimuli condition and least squares approximation is applied in order to find the terms of the

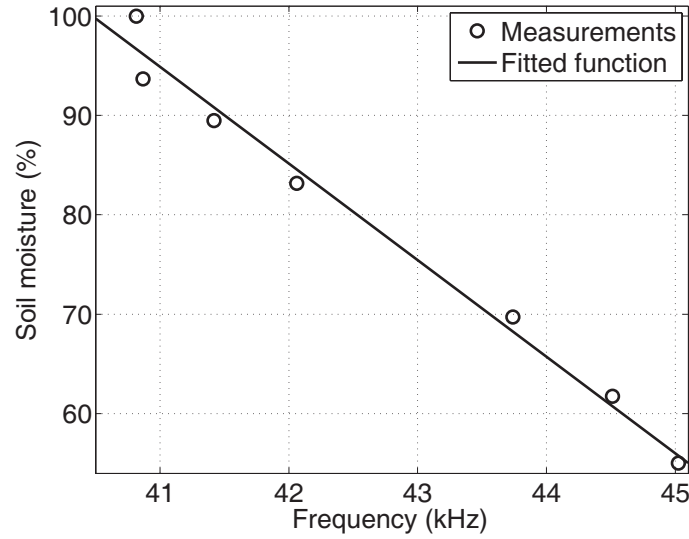


Figure 3.22: Measured soil moisture (%) characteristic and fitted function versus frequency.

polynomial.

In order to emulate different %SM conditions, a sample of soil was dried in a microwave oven and weighted. Flowingly, specific amount of water was poured and the %SM is calculated as follows:

$$\%SM = \frac{M_W - M_D}{M_D}, \quad (3.23)$$

where M_W and M_D is the mass (in grams) of the wet and dried soil sample, respectively. Fig. 3.22 depicts the transfer function and the %SM samples from a node for a soil moisture value of 55 – 95 %. It is prominent that frequency is almost a linear function of %SM. The subcarrier frequency data, collected during the calibration procedure (1500 samples), were input into the transfer function in order to characterize the measurement accuracy of the nodes. The %SM output of the transfer function was compared with the reference measurements. It was found that the nodes exhibit a root mean squared error (RMSE) and a mean absolute error (MAE) of 0.1 %SM and 0.08 %SM, respectively, which is sufficient for precision agriculture.

The theoretical relationship of the tag's frequency output value with the

%SM value can be calculated using (3.4). However, deviations from non-ideal values of the tag's components (e.g., tolerance of capacitors, resistors, timer, sensor etc) result in deviations from (3.4). In order to avoid those deviations, the calibration process is utilized for each tag.

The real-world application of a network with soil moisture sensors targets an *outdoor* field. Such environments exhibit great temperature variations, that significantly affect the operation of the electronic circuits within the tag. For example, the "CSS555" timer exhibits a temperature drift of 40 ppm/°C and, thus, for a tag with nominal subcarrier frequency 50 kHz, a total change of 15°C results to a frequency shift of 30 Hz. Hence, for a tag that occupies a bandwidth of 2 kHz, this frequency shift amounts to 1.5 % of the tag's bandwidth and a %SM error of the same order (in percentage). It's obvious that the %SM error is not important in our case so it is unnecessary to be compensated this effect with calibration process.

3.12 Ranges and Cost

A setup, which consists of a receiver, a node operating at 28.5 kHz and an emitter which produced a carrier wave (CW) with 20 mW power, was utilized in order to investigate the backscatter nodes' communication performance. The equipment was set up in bistatic topology with $d_{\text{et}} = 7.5$ m and $d_{\text{tr}} = 100$ m. The frequency value of the sensor was monitored using a data-logger and it was compared with the corresponding estimated frequency at the reader. An RMSE of 1.9 %SM was observed for a dataset of 1500 samples. The cost of each sensor in quantities of 1 is 5 € (the SMA connector is not included in the price, since the antenna will be integrated with the RF front-end in future designs).

3.13 Testbed

Finally a bistatic topology, testbed with two sensor nodes (sensors 1, 2 in Fig. 3.18) was installed in a basil plant in the lab (Fig. 3.23). The frequency data that was collected for a period 3 hours are illustrated in Fig. 3.24. It is

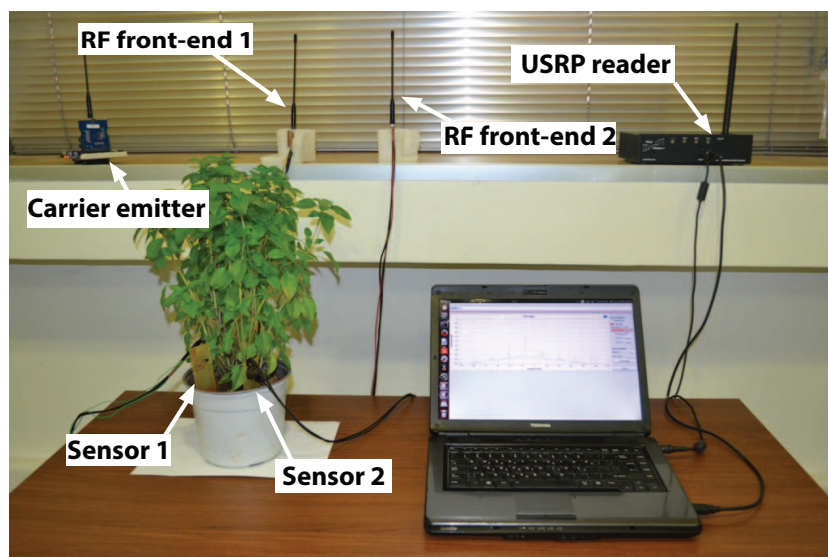


Figure 3.23: Indoor setup testbed of the bistatic analog backscatter architecture.

observed that after the watering instance, the output frequency of the nodes changes instantly, while it settles after approximately 20 minutes.

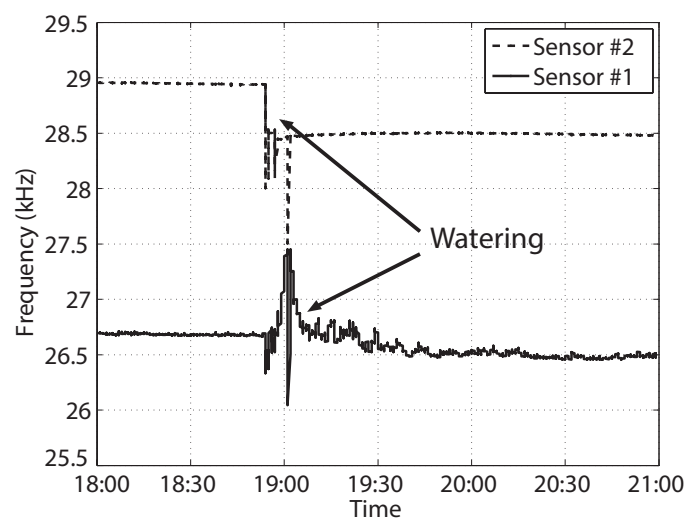


Figure 3.24: Soil moisture measurements of two sensors for 3 hours.

Chapter 4

Conclusions

4.1 Conclusion

In the first part of this thesis, a high efficiency, low-cost (with lossy FR-4 substrate), low-complexity (single diode in a series configuration) rectenna-grid is presented. The performance is evaluated via two ways; the rectifier is connected directly to a signal generator or the latter radiates through a log-periodic antenna and the rectenna grid receives energy at far-field. Measurements from both procedures agree with simulation and demonstrate high efficiency rectification, for low-power density, low-power input and low-cost. Emphasis was given on collecting and offering as much power as possible at the load. Finally, the rectenna was connected to a DC-to-DC converter and the energy stored in a capacitor is able to supply a node.

The second part develops a sensor network node that costs 5 € and consumes power on the order of 100 μ W. The backscatter sensor nodes consists of a CtF implemented with a 555 timer that can be connected with two sensing elements, a custom capacitive soil moisture sensor and a plant signal sensor. Soil moisture sensor was selected to be embedded on the tag. Soil moisture is frequency modulated and the voltage pulses of the converter are driven to the single-switch RF front-end that implements scatter-radio communication. The scattered signals are received by the SDR reader that converts frequency to %SM via a carefully calculated calibration function. Soil moisture is measured by the nodes with an RMSE and MAE on the order of 0.1 and 0.08 %SM respectively. For communication range of $d_{et}=7.5$ m and $d_{tr}=100$ m the RMSE is on the order of 1.9 %SM. For the networking capability, the sensors utilize an FDMA scheme that is implemented via the installation of specific passive components on each node.

4.2 Future Work

Future work could target to extend the capabilities of the developed system in terms of scale, greater communication range and even power. About the scale, efforts will focus on developing and deploying an ultra large scale network of such sensor nodes. Finally the goal is to be designed battery-less sensor nodes embedded with RF power harvesters so they may be powered wirelessly. In the wireless powering system, a single emitter or a network of them will power multiple sensor devices. Power harvester receivers embedded inside the sensor nodes will receive RF energy up to 7 meters away from the emitters broadcasting radio waves at 868 MHz.

Appendix

Table 4.1: Plant signal sensor bill of materials.

| # | Qty. | Schematic ID | Description | Man. ID |
|---|------|-------------------------------|----------------------------------|--------------------|
| 1 | 5 | R1, R2, P3, R4, R5 | Res., 100 k Ω , 603, | RC0603JR-07100KL |
| 2 | 2 | R6, R7 | Res., 50 k Ω , 603, | ERA-3AEB154V |
| 3 | 2 | R8, R9 | Trimmer Res., 100 k Ω , , | 3314G-1-104E |
| 4 | 1 | IC1 | IC OPAMP MCP6044 TSSOP14 | MCP6044T-1/STCT-ND |
| 5 | 6 | V1, V2, RFIN, VOUT, VREF, GND | 2x1 DIP Header | SSA-132-S-T |

Table 4.2: Tag bill of materials.

| # | Qty. | Schematic ID | Description | Man. ID |
|----|------|------------------|-------------------------|-------------------|
| 1 | 4 | C1, C2, C3, C9 | Cap., 0.1 μ F, 603, | C0805C104K3RACTU |
| 2 | 2 | C4, C10 | Cap., 1 μ F, 1206 | C0805C105K8RACTU |
| 3 | 1 | BAT1 | CR2032 Batt. Holder | BS-7 |
| 4 | 2 | JP_POW, JP_PV1 | 2x1 DIP Header | SSA-132-S-T |
| 5 | 2 | U_R1_SWITCH | IC Switch SPDT 6-TSSOP | SN74LVC1G3157DCKR |
| 6 | 1 | D_VREF | Voltage Ref. IC | REF3018AIDBZT |
| 7 | 1 | U7555 | CSS555 Timer IC | CSS555-ID |
| 8 | 2 | R_555_1, R_555_2 | Timing Res. | N/A |
| 9 | 2 | C5, C6, C7 | Timing Cap. | N/A |
| 10 | 1 | ADG919 | RF Switch 8-MSOP | ADG919BRMZ-ND |
| 11 | 1 | L_1, | RF Chocke | BLM18GG471SN1D |
| 12 | 1 | JP_SMA | SMA RF Conn. | 142-0701-806 |
| 13 | 2 | JP_1, JP_2, JP_3 | 2x1 DIP Header | SSA-132-S-T |

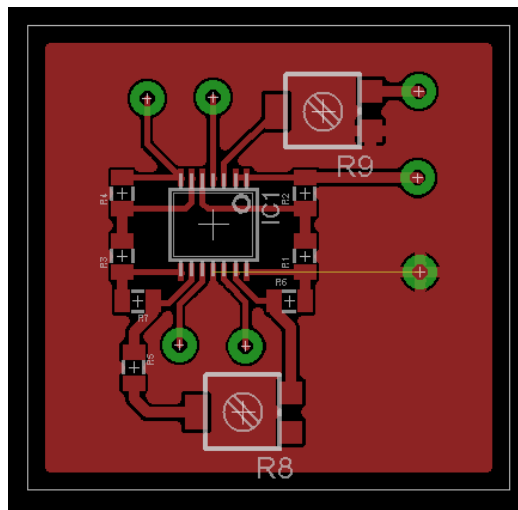
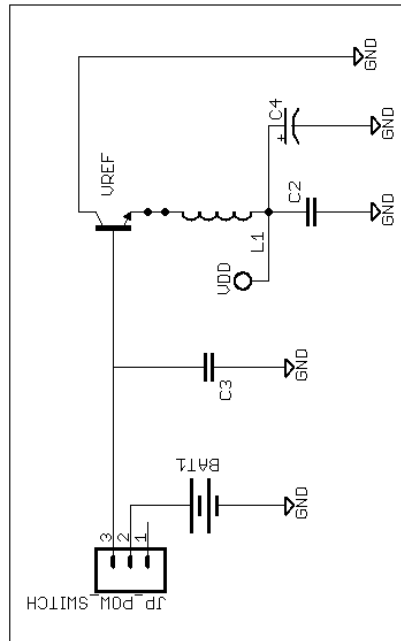


Figure 4.2: PCB layout of plant signal sensor.

Power Supply Circuit



Analog Frequency Modulator Circuit

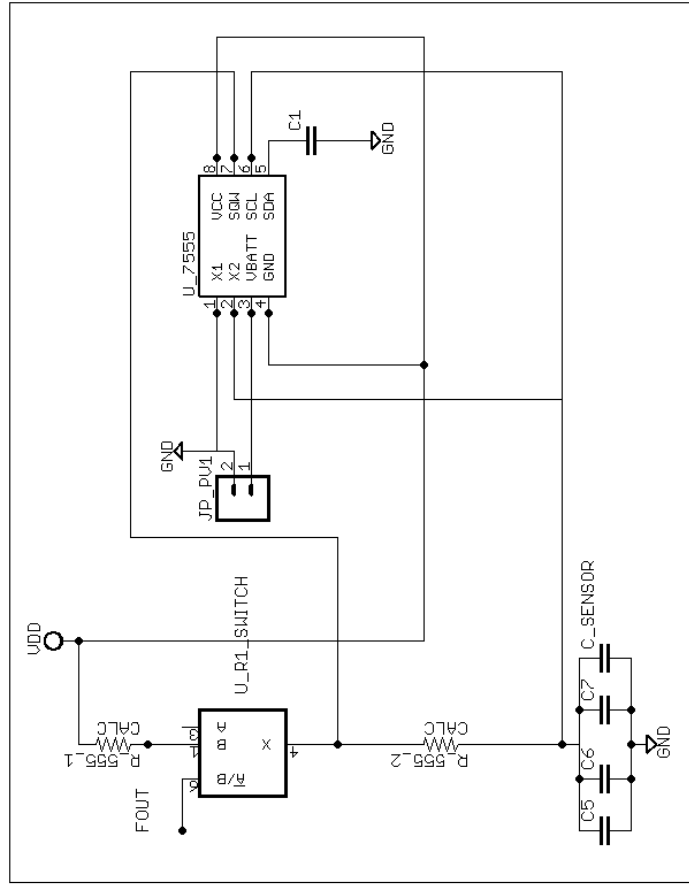


Figure 4.3: Schematic of timer module, soil moisture sensor and power supply circuit.

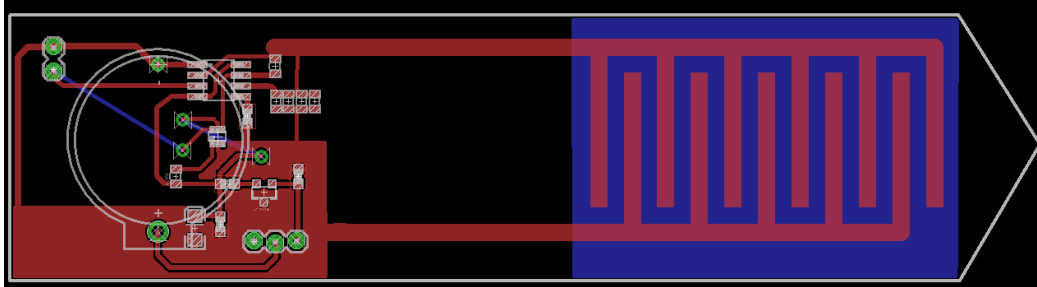


Figure 4.4: PCB layout of timer module, soil moisture sensor and power supply circuit.

RF Front-end

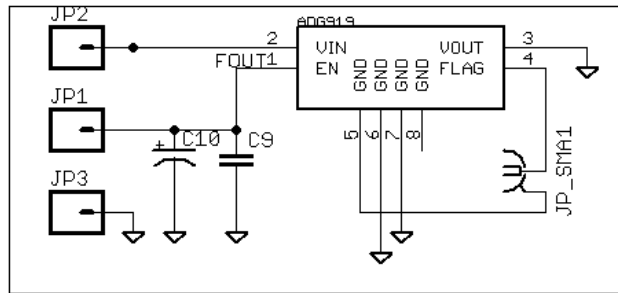


Figure 4.5: Schematic of RF front-end.

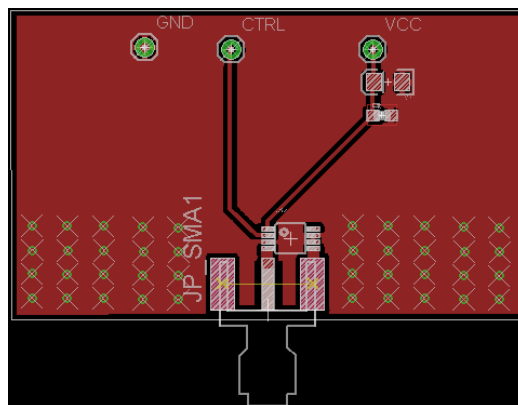


Figure 4.6: PCB layout of RF front-end.

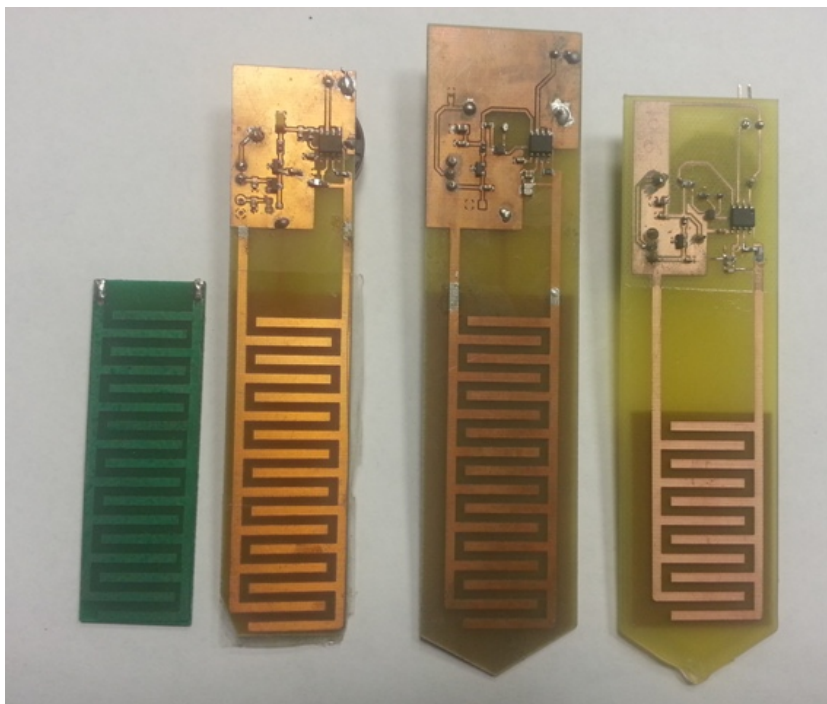


Figure 4.7: The various tag and sensor prototypes that were fabricated.

Bibliography

- [1] *MIMOS Patent Pending*, Dr. Agus Santoso Tamsir, Dzuzlindah Muhamad Alias, Azrif Manut, Suraya Sulaiman and Meilana Siswanto.
- [2] K. Lin, J. Yu, J. Hsu, S. Zahedi, D. Lee, J. Friedman, A. Kansal, V. Raghunathan, and M. Srivastava, “Heliomote: enabling long-lived sensor networks through solar energy harvesting,” in *3rd Int. Conf. Embedded Networked Sensor Syst.*, ACM, 2005, p. 309.
- [3] N. Tesla, “The transmission of electrical energy without wires,” *Electrical World and Engineer*, vol. 1, 1904.
- [4] J.-P. Curty, M. Declercq, C. Dehollain, N. Joehl, M. Declercq, and M. Declercq, *Design and optimization of passive UHF RFID systems.*, Springer, 2007.
- [5] S. D. Assimonis and A. Bletsas, “Energy harvesting with a low-cost and high efficiency rectenna for low-power input,” in *IEEE Radio Wireless Week 2014*, Newport Beach, CA, USA January 2014.
- [6] G. Tolle, J. Polastre, R. Szewczyk, D. Culler, N. Turner, K. Tu, S. Burgess, T. Dawson, P. Buonadonna, D. Gay, and W. Hong, “A macroscope in the redwoods,” in *Proceedings of the 3rd International Conference on Embedded Networked Sensor Systems*, ser. SenSys '05, 2005.
- [7] W.-Z. Song, R. Huang, M. Xu, B. Shirazi, and R. LaHusen, “Design and deployment of sensor network for real-time high-fidelity volcano monitoring,” *IEEE Transactions on Parallel and Distributed Systems*, vol. 21, no. 11, pp. 1658–1674, 2010.

-
- [8] Y. Liu, Y. He, M. Li, J. Wang, K. Liu, L. Mo, W. Dong, Z. Yang, M. Xi, J. Zhao, and X.-Y. Li, “Does wireless sensor network scale? a measurement study on greenorbs,” in *INFOCOM, 2011 Proceedings IEEE*, Shanghai, China, 2011.
- [9] L. Mottola and G. P. Picco, “Programming wireless sensor networks: Fundamental concepts and state of the art,” *ACM Computer. Surv.*, vol. 43, no. 3, pp. 19:1–19:51, Apr. 2011.
- [10] A. Sample, D. Yeager, P. Powledge, and J. Smith, “Design of a passively-powered, programmable sensing platform for uhf rfid systems,” in *IEEE International Conference on RFID 2007*, Mar. 2007, pp. 149–156.
- [11] G. Vannucci, A. Bletsas, and D. Leigh, “A software-defined radio system for backscatter sensor networks,” *IEEE Trans. Wireless Commun.*, vol. 7, no. 6, pp. 2170–2179, Jun. 2008.
- [12] V. Lakafosis, A. Rida, R. Vyas, L. Yang, S. Nikolaou, and M. Tentzeris, “Progress towards the first wireless sensor networks consisting of inkjet-printed, paper-based rfid-enabled sensor tags,” *Proceedings of the IEEE*, vol. 98, no. 9, pp. 1601–1609, Sep. 2010.
- [13] D. Cirmirakis, A. Demosthenous, N. Saeidi, and N. Donaldson, “Humidity-to-frequency sensor in CMOS technology with wireless read-out,” *IEEE Sensors Journal*, vol. 13, no. 3, pp. 900–908, 2013.
- [14] W. C. Brown, “The history of power transmission by radio waves,” *IEEE Trans. Microw. Theory Techn.*, vol. 32, no. 9, pp. 1230–1242, 1984.
- [15] J. Zbitou, M. Latrach, and S. Toutain, “Hybrid rectenna and monolithic integrated zero-bias microwave rectifier,” *IEEE Trans. Microwave Theory Tech.*, vol. 54, no. 1, pp. 147–152, 2006.
- [16] J. A. Hagerty, F. B. Helmbrecht, W. H. McCalpin, R. Zane, and Z. B. Popovic, “Recycling ambient microwave energy with broad-band rectenna arrays,” *IEEE Trans. Microwave Theory Tech.*, vol. 52, no. 3, pp. 1014–1024, 2004.

-
- [17] J.-Y. Park, S.-M. Han, and T. Itoh, "A rectenna design with harmonic-rejecting circular-sector antenna," *IEEE Antennas Wireless Propag. Lett.*, vol. 3, no. 1, pp. 52–54, 2004.
- [18] E. Falkenstein, M. Roberg, and Z. Popovic, "Low-power wireless power delivery," *IEEE Trans. Microwave Theory Tech.*, vol. 60, no. 7, pp. 2277–2286, 2012.
- [19] J. Akkermans, M. Van Beurden, G. Doodeman, and H. Visser, "Analytical models for low-power rectenna design," *IEEE Antennas Wireless Propagat. Lett.*, vol. 4, pp. 187–190, 2005.
- [20] R. J. Vyas, B. B. Cook, Y. Kawahara, and M. M. Tentzeris, "E-WEHP: A batteryless embedded sensor-platform wirelessly powered from ambient digital-tv signals," *IEEE Trans. Microw. Theory Techn.*, vol. 61, no. 6, pp. 2491–2505, 2013.
- [21] A. Costanzo, A. Romani, D. Masotti, N. Arbizzani, and V. Rizzoli, "Rf/baseband co-design of switching receivers for multiband microwave energy harvesting," *Sensors and Actuat. A: Phys.*, vol. 179, pp. 158–168, 2012.
- [22] H. Sun, Y.-x. Guo, M. He, and Z. Zhong, "Design of a high-efficiency 2.45-ghz rectenna for low-input-power energy harvesting," *IEEE Antennas Wireless Propagat. Lett.*, vol. 11, pp. 929–932, 2012.
- [23] A. Collado and A. Georgiadis, "Conformal hybrid solar and electromagnetic (EM) energy harvesting rectenna," *IEEE Trans. Circuits Syst. I*, vol. 60, no. 8, pp. 2225–2234, 2013.
- [24] A. Georgiadis, G. Andia, and A. Collado, "Rectenna design and optimization using reciprocity theory and harmonic balance analysis for electromagnetic (EM) energy harvesting," *IEEE Antennas Wireless Propag. Lett.*, vol. 9, pp. 444–446, 2010.

-
- [25] C. Mikeka, H. Arai, A. Georgiadis, and A. Collado, "Dtv band micropower rf energy-harvesting circuit architecture and performance analysis," in *IEEE Int. RFID-Technol. Appl. Conf.*, IEEE, 2011, pp. 561–567.
- [26] M. Piñuela, P. D. Mitcheson, and S. Lucyszyn, "Ambient rf energy harvesting in urban and semi-urban environments," *IEEE Trans. Microwave Theory Tech.*, vol. 61, no. 7, pp. 2715–2726, 2013.
- [27] Y. Kawahara, H. Lee, and M. M. Tentzeris, "Sensprout: inkjet-printed soil moisture and leaf wetness sensor," in *ACM Conf. on Ubiquit. Comp.*, Sept. 2012, pp. 545–545.
- [28] S. Kim, Y. Kawahara, A. Georgiadis, A. Collado, and M. Tentzeris, "Low-cost inkjet-printed fully passive rfid tags using metamaterial-inspired antennas for capacitive sensing applications," in *IEEE MTT-S Int. Microw. Symp. Dig.*, Jun. 2013, pp. 1–4.
- [29] E. Kampianakis, J. Kimionis, K. Tountas, C. Konstantopoulos, E. Koutroulis, and A. Bletsas, "Wireless environmental sensor networking with analog scatter radio and timer principles," *IEEE Sensors J.*, accepted for publication.
- [30] S. D. Assimonis, E. Kampianakis, and A. Bletsas, "Microwave analysis and experimentation for improved backscatter radio," in *IEEE Europ. Conf. on Antennas and Prop.*, Apr. 2014.
- [31] C.-T. Sah, C.-T. Sah, and C.-T. Sah, *Fundamentals of solid-state electronics.*, World Scientific Singapore, 1991, vol. 437.
- [32] S. Wetenkamp, "Comparison of single diode vs. dual diode detectors for microwave power detection," in *Microwave Symposium Digest, 1983 IEEE MTT-S International.*, IEEE, 1983, pp. 361–363.
- [33] A. J. Cardoso, M. Schneider, and C. Montoro, "Design of very low voltage cmos rectifier circuits," in *Circuits and Systems for Medical and Environmental Applications Workshop (CASME), 2nd.*, IEEE, 2010, pp. 1–4.

-
- [34] A. J. Cardoso, L. G. de Carli, C. Galup-Montoro, and M. C. Schneider, "Analysis of the rectifier circuit valid down to its low-voltage limit," *Circuits and Systems I: Regular Papers, IEEE Transactions on*, vol. 59, no. 1, pp. 106–112, 2012.
- [35] *Data sheet HSMS-285x*, 1st ed., Avago Technologies, 2012, available online: <http://www.avagotech.com>.
- [36] S. Adami, V. Marian, N. Degrenne, C. Vollaie, B. Allard, and F. Costa, "Self-powered ultra-low power dc-dc converter for rf energy harvesting," in *IEEE Faible Tension Faible Consommation.*, IEEE, 2012, pp. 1–4.
- [37] H. Stockman, "Communication by means of reflected power," *Proc. IRE*, pp. 1196–1204, 1948.
- [38] D. M. Dobkin, *The RF in RFID: Passive UHF RFID in Practice.*, Newnes (Elsevier), 2008.
- [39] J. Kimionis, A. Bletsas, and J. N. Sahalos, "Bistatic backscatter radio for tag read-range extension," in *IEEE International Conference on RFID-Technologies and Applications (RFID-TA)*, Nice, France, Nov. 2012.
- [40] J. Kimionis, A. Bletsas, and J. N. Sahalos, "Design and implementation of RFID systems with software defined radio," in *Proc. IEEE EUCAP*, Prague, Czech Republic, Mar. 2012, pp. 3464–3468.
- [41] J. Kimionis, A. Bletsas, and J. N. Sahalos, "Increased range bistatic scatter radio," *IEEE Trans. Commun.*, vol. 62, no. 3, pp. 1091–1104, Mar. 2014.
- [42] E. Kampianakis, J. Kimionis, C. Konstantopoulos, E. Koutroulis, and A. Bletsas, "Backscatter sensor network for extended ranges and low cost with frequency modulators: Application on wireless humidity sensing," in *Proc. IEEE Sensors*, Baltimore, USA, Nov. 2013.
- [43] E. Kampianakis, J. Kimionis, C. Konstantopoulos, E. Koutroulis, and A. Bletsas, "Wireless environmental sensor networking with analog scat-

-
- ter radio & timer principles,” *IEEE Sensors J.*, submitted for publication.
- [44] A. Bletsas, A. G. Dimitriou, and J. N. Sahalos, “Improving backscatter radio tag efficiency,” *IEEE Trans. Microwave Theory Tech.*, vol. 58, no. 6, pp. 1502–1509, Jun. 2010.
- [45] K. Sundara-Rajan, A. V. Mamishev, and M. Zahn, “Fringing electric and magnetic field sensors,” *Encyclopedia of Sensors*, vol. 10, pp. 1–12, 2005.
- [46] X. B. Li, S. D. Larson, A. S. Zyuzin, and A. V. Mamishev, “Design principles for multichannel fringing electric field sensors,” *Sensors Journal, IEEE*, vol. 6, no. 2, pp. 434–440, 2006.
- [47] A. V. Mamishev, S. R. Cantrell, Y. Du, B. C. Lesieutre, and M. Zahn, “Uncertainty in multiple penetration depth fringing electric field sensor measurements,” *Instrumentation and Measurement, IEEE Transactions on*, vol. 51, no. 6, pp. 1192–1199, 2002.
- [48] S. Mancuso, “Hydraulic and electrical transmission of wound-induced signals in *vitis vinifera*,” *Functional Plant Biology*, vol. 26, no. 1, pp. 55–61, 1999.
- [49] J. Fromm and H. Fei, “Electrical signaling and gas exchange in maize plants of drying soil,” *Plant Science*, vol. 132, no. 2, pp. 203–213, 1998.
- [50] J. FROMM and S. Lautner, “Electrical signals and their physiological significance in plants,” *Plant, Cell & Environment*, vol. 30, no. 3, pp. 249–257, 2007.
- [51] P. M. Gil, L. Gurovich, B. Schaffer, J. Alcayaga, S. Rey, and R. Iturriaga, “Root to leaf electrical signaling in avocado in response to light and soil water content,” *Journal of plant physiology*, vol. 165, no. 10, pp. 1070–1078, 2008.

-
- [52] P. Oyarce and L. Gurovich, “Electrical signals in avocado trees: Responses to light and water availability conditions,” *Plant signaling & behavior*, vol. 5, no. 1, pp. 34–41, 2010.
- [53] S. W. Smith, *The scientist and engineer’s guide to digital signal processing.*, California Technical Publishing, San Diego, 1997.
- [54] A. Bletsas, S. Siachalou, and J. N. Sahalos, “Anti-collision backscatter sensor networks,” *IEEE Trans. Wireless Commun.*, vol. 8, no. 10, pp. 5018–5029, Oct. 2009.
- [55] P. Stoica and R. Moses, *Spectral analysis of signals.*, Prentice-Hall International, 1st ed., 2005.
- [56] J. Fraden, *Handbook of modern sensors.*, Springer, 2010.
- [57] J. Fan and I. Gijbels, *Local polynomial modelling and its applications.*, Chapman and Hall/CRC, 1996.